MODIS-based climate monitoring and snow cover modeling in the area of Deadhorse/Prudhoe Bay, Alaska

Tarek Kemper[1]

[1]Department of Geography, Humboldt-University of Berlin, Rudower Chaussee 16, 12489 Berlin

Correspondence: Tarek Kemper (kemperta@hu-berlin.de)

Contents

List of Figures

List of Tables

Abstract. Detailed knowledge about ground surface conditions is crucial for monitoring the thermal state of permafrost and dynamics in active layer thickness. In vast areas such as the high arctic latitudes of northern Alaska, where observational data are sparse, remote sensing has proved to afford opportunities in detecting surface conditions. In order to detect peak snow water equivalents (SWE), this study presents an approach that makes use of Moderate Resolution Imaging Spectroradiometer (MODIS) land surface temperatures (LST), NDSI snow cover and albedo for downscaling ERA reanalysis data by the means of an SEB-scheme. Furthermore, MODIS-derived data sets are used to give an overview on the general climatic conditions in the area of Deadhorse/Prudhoe Bay, Alaska. Over the period from 2003 till 2016 LST show an increasing trend for every pixel in the about 6500km² large study area. Major warming trends of up to 0.1K per year appear next to the coast and in flat inland regions. The mean annual snow-offset date discovered by MODIS happens about 9 days erlier at the end of the study period. The SEB-scheme provides feasible results of annual peak SWE with a mean value of 0.31 $mSWE$ for the entire study area (over the ERA-5 period 2010-2016). The resulting peak-SWE maps can be utilized to detect specific prevailing conditions in the study area as well as they demonstrate the high spatial variability of snow cover in 500m spatial resolution. The two reanalysis products ERA-5 and ERA-Interim have been found to act differently due to the large difference in grid spacing, especially in coastal regions. Since the scheme is strongly dependent on the length of the snowmelt period, especially inaccuracies in the MODIS-based complete snowmelt date can lead to uncertainties.

1 Introduction

In the face of a warming climate, much of the global permafrost[1] experiences warming and thawing processes (Zhang et al., 1997; Osterkamp, 2003a). Borehole measurements have revealed an increasing and sustained warming trend in temperatures beneath the ground surface for several decades (Romanovsky et al., 2008). Since permafrost is strongly dependent on ground surface conditions, snow cover is, among the near surface temperature, the most important influencing factor (Goodrich, 1982). In addition to that, inaccurate knowledge on snow cover leads to large uncertainties in permafrost monitoring (Langer et al., 2013). Numerous studies suggest that differing timing and duration of snow coverage have strong influences on ground surface temperatures (Ling and Zhang, 2003; Zhang, 2005). The insulating effect, which seasonal snow cover has on the ground surface, strongly affects the permafrost's thermal regime and active layer (Ling and Zhang, 2003). Generally, at locations where significant snow cover is existing, mean annual air temperatures (MAAT) are lower than mean annual ground surface temperatures (MAGST) due to this insulating effect. Furthermore, it has been demonstrated that terrestrial ecosystems are very sensitive to snow cover variations (Stone et al., 2002) due to its impacts on the surface energy budget (a decrease of days with snow cover means lower surface albedo and therefore more absorption). The snow cover is also affecting the vegetation period. The magnitude at which snow cover affects the ground thermal regime is dependent on numerous factors. As mentioned before, timing and duration play an important role, but also density and structure, and interactions between snow cover and local microrelief. Also, the overall geographic location with accumulation or wind drift effects, influences the magnitude of snow cover's effect on MAGST (Zhang, 2005). For instance, Sturm and Holmgren (1994) present snow depth differences of several centimeters within less than a meter of spatial extent. In addition to that, snow cover's spatial extent varies greatly with the seasons (Frei et al., 2012). Thus, snow cover and its thermal properties were reported to be the largest source of uncertainty (Langer et al., 2013) in monitoring permafrost. To understand the future evolution of permafrost, its thermal regime and active layer dynamics, a widespread and consistent monitoring network throughout the entire Arctic would be needed (Lindsay et al., 2015). Since permafrost covers about a quarter of the land area in the northern hemisphere (Anisimov and Nelson, 1996), its degradation has widespread consequences such as build-up of thermokarst or the destabilization of former solid surfaces. Ecosystem processes such as controlling the soil temperature and moisture, rooting zones and subsurface hydrology depend on permafrost (Jorgenson et al., 2001). Permafrost degradation can have impacts on terrestrial or solid ecosystems that might be converted into wetland or aquatic systems (Osterkamp et al., 2000). This is closely linked with the release of greenhouse gases out of organic-rich permafrost (Schuur and Abbott, 2011), thus, further accelerating climate warming itself. Furthermore, permafrost builds the physical basis for infrastructure such as streets or buildings in communities and, finally, thawing permafrost has an impact on industrial sites in the high arctic. Several studies have already reported about changes in the thermal state of permafrost with increasing temperatures over a few decades. For instance, Osterkamp and Romanovsky (1999) reported about up to 1.5°C increase between the late 1980s and 1996 in northern Alaska. Osterkamp (2003c) display similar trends over a longer time period (late 1970s till 2002). It is suggested that this warming trend will proceed throughout the 21st century (Anisimov et al., 2007; Zhang et al., 2014). Thus, further affecting the terrestrial landscape by altering plant communities and local biodiversity, redistribution of surface waters, and altering wildlife use; organic matter accumulation, and the emergence of new sources and sinks of climate-relevant trace

[1] Permafrost is defined as any material beneath the ground surface that remains frozen for at least two consecutive years (Van Everdingen, 1998).

gases (Jorgenson et al., 2006). These findings highlight the need of more detailed information on the differing influencing factors such as vegetation, MAGST, and snow cover. The spatial variety of these factors leads to diverse response and sensitivity of permafrost. In the past decades, numerous measurements of climate variables related to permafrost have been conducted in different parts of the Arctic (Romanovsky et al., 2010; Smith et al., 2010; Langer et al., 2011; Westermann et al., 2016). A global network of permafrost observatories, the GTN-P[2], has been designed to address the monitoring of changes in permafrost active-layer thickness and its thermal state. However, a frequently prevailing harsh climate in these vast areas makes conducting and especially maintaining in-situ measurements difficult and logistically cost-intensive and still turns large parts of the Arctic into data-sparse regions (Hachem et al., 2012; Clow, 2014). Where ground-based measurements are absent, remotely-sensed datasets may be available. Remote sensing has turned out to be a useful tool to retrieve a large amount of surface datasets of climate variables such as snow cover (Frei et al., 2012; Lindsay et al., 2015) and land surface temperatures (Hachem et al., 2012). But since permafrost is a subsurface phenomenon, it is not possible to monitor permafrost's thermal regime and active layer thickness with remote-sensing as stand-alone product. This is especially crucial for regions where snow covers the ground surface for up to 9 months per year (Ling and Zhang, 2003), making it impossible to observe ground surface temperatures and conditions. Nonetheless, satellite-based surface datasets can be implemented in land-surface schemes, which are able to represent the thermal state of permafrost. In terms of permafrost modeling Langer et al. (2013) applied weekly averages of MODIS-based LST and fractional snow cover (fsc) in combination with GlobSnow SWE as forcing for a transient permafrost model at specific point locations in the Lena-River-Delta (LRD) in NE Siberia. The study shows that satellite-derived forcing leads to feasible performances, such as reproducing warming trends of permafrost temperatures. However, limitations arise through implementation of the satellite snow product with a 25 km resolution, similarly operates little knowledge about the thermal properties of snow cover. Others used different surface features characteristic for permafrost landscapes to measure changes in permafrost's thermal state such as the quantification of pond and thermokarst lake dynamics (Jones et al., 2011) or the investigation of correlative relationships between near-surface permafrost and topographic or vegetational features (Panda et al., 2010, 2014). Combining field observations with remotely-sensed data is a common approach to derive information about permafrost conditions, but still, widespread utilization depends on the availability of in-situ observations. Different approaches to indicate permafrost dynamics in Alaska rely on combined ground-based measurements with downscaled 2 km resolution climate data (Jafarov et al., 2012) or modelling based on interpolation of observational data sets (Westermann et al., 2013). Westermann et al. (2017) utilize remotely-sensed data (MODIS LST, MODIS snow extent and GlobSnow SWE) in combination with reanalysis data from ERA-Interim to estimate active layer thickness and transient evolution of the thermal state of permafrost for a 16.000 km² site in the LRD. By comparison to in-situ observations the satellite-based model scheme yields feasible results, except for limitations and deficiencies of currently available remotely-sensed snow measurements. Many approaches have been demonstrated to address the uncertainties arising from inaccurate knowledge on snow conditions, for instance, Pulliainen (2006) demonstrated an assimilation technique that is based on space-born data and ground measurements. This approach displayed that the combination of ground-based data and space-borne radiometer observations reduces systematic errors in SWE and snow depths measurements. An ensemble-based assimilation approach is demonstrated by Aalstad et al. (2017). For estimating peak SWE at the kilometer scale they make use of MODIS and Sentinel-2 datasets as well as ERA-Interim data as forcing for a simple snow model. Molotch and Margulis (2008) present an approach that reconstructs SWE by the means of spatially distributed snowmelt model, which is driven by time series from several remote sensing products (i.a. MODIS). They found that SWE estimates based on Landsat ETM+ data offer the best results, despite of the reduced temporal resolution (compared to MODIS). However, they propose that future reconstructions of SWE can be based on improved MODIS products and therefore at a higher temporal scale. In the following I introduce an approach that utilizes both MODIS NDSI snow cover and albedo data in high spatial resolution and ERA-reanalysis datasets in high temporal resolution to create SWE time series for a study area around Deadhorse/Prudhoe Bay in Alaska's North Slope Territory. Within this approach, no in-situ measurements are utilized. This is conducted by the means of a surface-energy-balance (SEB) scheme that downscales ERA reanalysis data with MODIS. The first chapter introduces the study area, followed by a comprehensive description of the utilized datasets that were used for the computations as well as for comparison. The methodology part guides step-by-step through the applied scheme and after that, the results for both a general climate overview of the study area based on MODIS and the SWE outcomes are presented. In the following chapter the scheme's performance is discussed regarding strengths, weaknesses and limitations as well as improvements. The paper closes with a summarizing conclusion that also gives an outlook on possible proceedings.

[2]https://gtnp.arcticportal.org/

2 Study Area

The study region covers an area of approx. 6500 km² in Alaska's North Slope Territory including 5 observational sites, from north to south West Dock, Deadhorse/Prudhoe Bay, Franklin Bluffs, Sagwon and Happy Valley (cf. Fig. 1). The study area is entirely located in continuous permafrost zone, between the Beaufort Sea and the Brooks Range. The entire study area represents the arctic tundra biome, with a maritime climate next to the coast and a more continental climate towards inland (Zhang et al., 1996; Romanovsky et al., 2008). The coastal zone experiences more frequent cloudiness and fog during summer seasons, whereas clear-sky conditions are more prevalent inland (Zhang et al., 1996). MAAT vary between up to -12°C near the coast and about -10°C at the foothills of the mountains, based on long-term measurements since the mid-1980s (Romanovsky et al., 2008). Minimum and maximum temperature within a year were observed to range as much as 60°C, primarily at the inland sites (Osterkamp, 2003c). Overall, air temperatures remain below zero for up to 9 months per year (Zhang et al., 1997). Air temperatures were observed to increase over the past decades everywhere in the study area. For instance, Romanovsky et al. (2003) demonstrated a warming trend of about 1.5°C for a 16-year period in Deadhorse. Seasonal variability in air temperatures appears to be larger at the sites in inland direction. Differences between MAAT and MAGST were reported to be highest during the winter months (October-May), where snow cover's insulating effect on the ground surface is strongest (Zhang et al., 1997). For the period of 1984 till 2001 Osterkamp (2003b) reported the MAGST to be about 6°C higher than the MAAT. In winter 1988 the difference between MAGST and MAAT was measured as high as 36.3°C in Franklin Bluffs (Zhang, 2005). Spatial differences in MAGST appear to be much larger than differences in MAAT along the transect which originates from distinct surface conditions, primarily snow cover, vegetation and micro-topography (Romanovsky et al., 2008). At the same time, GST have increased in a similar magnitude as the air temperatures, especially over multi-year averages (Romanovsky et al., 2003). However, Romanovsky et al. (2003) demonstrate, that for instance in the two consecutive years 1990 and 1991 the evolution of GST was inverse compared to the air temperatures. It is most likely, that snow cover thickness and its interannual variability affected these diverging temperature evolutions. Snow-covered seasons normally last from October till May, with a slightly decreasing season-length towards inland sites (Zhang et al., 1996). Further snow properties reveal similar gradients so that snow thickness increases from north to south, whereas snow density decreases in the same direction (Zhang et al., 1996; Romanovsky et al., 2003). Snow thickness has a large impact on the behavior of ground surface temperatures, so that GST in West Dock follow the air temperatures much more consistently than at the other sites. Snow-free seasons usually endure about 4 months, with a large variation in first day of seasonal snow cover onset. Snow cover disappearance is reported to be up to 3 weeks earlier along the coast leading to longer snow-free periods at the inland sites (Zhang et al., 1996). Stuefer et al. (2012) report that within a study between 2011 and 2012 snowmelt-onset happened in mid-May, whereas complete snowmelt was observed in early-June. Permafrost temperatures are demonstrated to be colder next to the coast than at the inland sites and similar to above ground surface temperatures demonstrated to be increasing (Romanovsky et al., 2003). There is a large spatial variety of permafrost's response to interannual changes in air temperatures, due to overall conditions at specific sites such as the geographical location, thermal properties of the soils and vegetation. Typically, permafrost extends to depths up to 600 meters in the area of Prudhoe Bay (Jorgenson et al., 2008) with a decrease in depth in southward direction. Equal to air and ground surface temperatures, permafrost temperatures increased by more than 1°C since the mid-1980s (Romanovsky et al., 2003). As mentioned before, the study area is located in arctic tundra biome representing different subzone types which Zhang et al. (1996) suggest to be divided into three major climatic zones: arctic foothills, arctic inland and arctic coastal. This classification is mainly based on the geographical location, vegetation and climatic conditions. In West Dock small grasses occur sporadically in wet arctic tundra, whereas moist non-acidic tundra is found at the Deadhorse and Franklin Bluffs sites. The sites towards the southern boundary of the study area are located in moist acidic tundra and feature moss with grass tussocks and partially even knee-high shrubs (Walker, 2000; Romanovsky et al., 2008). The differences in vegetation as well as in soil type have been shown to affect active layer temporal variations, so that Franklin Bluffs reveals the deepest measured active layer, decreasing in both northward and southward direction (Walker et al., 1998). Although the height difference between the 5 observational sites is only about 300m, the study area is characterized by a heterogenous landscape with small elevations in the center of the study site and numerous periglacial landforms such as pingos, various types of patterned ground and ice-wedge polygons, that indicate ice-rich permafrost (Raynolds et al., 2014). Since air temperatures, ground surface temperatures, and permafrost temperatures show increasing trends, this will hugely affect ecosystems, industries, and communities at the surface. Normally, these high arctic latitudes in Alaska are vast and relatively unpopulated areas, but since the late 1960s, where large petroleum reserves were discovered at the Alaskan coast of the Beaufort Sea, Prudhoe Bay has been one of the most intense ice-rich permafrost exploration sites (Lachenbruch et al., 1982). At the same time, Prudhoe Bay is the largest oilfield in the United States and was the first developed oil field in the entire Arctic (Raynolds et al., 2014), what led to a quickly growing, extensive infrastructure network around Deadhorse and

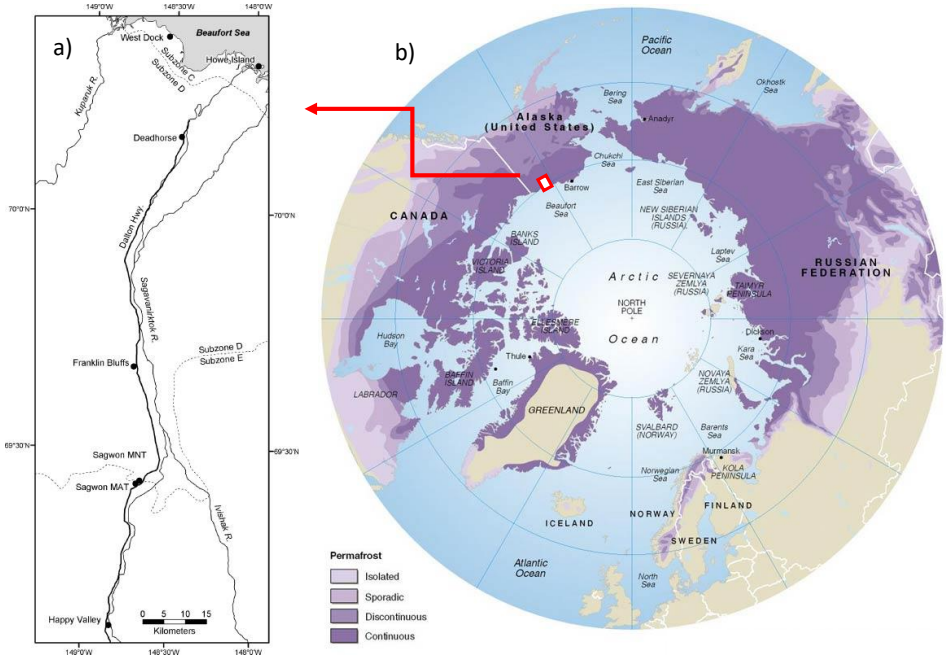

Figure 1. Study area. Figure a) shows the 5 observational sites extending from the coastal zone next to the Beaufort Sea (West Dock) to the foothills of the Brooks Range (Happy Valley). Except for West Dock, all sites are located next to the Saganavirktok River and Dalton Highway (Romanovsky et al., 2003). Figure b) displays the permafrost distribution on the northern hemisphere[a] and demonstrates that the entire study area is located in continuous permafrost.

[a]https://nsidc.org/cryosphere/frozenground/whereis_fg.html

Prudhoe Bay. Build-up of roads and buildings, or pumping of hot oil pose an additional threat to the sensitive environment.

3 Data base

The data base includes remotely-sensed data from MODIS, reanalysis data from ECMWF's ERA-Interim and ERA-5, and in-situ measurements from 5 observation sites[3] in the study area (cf. Tbl. 1).

3.1 Observation data sets

At some of the observation sites meteorological measurements have been conducted for more than 35 years (e.g. Lachenbruch et al. (1982)) and at all 5 of them at least small climate stations have been established. At most of the sites, air temperatures (in 1-3m height), above ground surface temperatures and borehole temperatures were measured over the period from 2003 till 2016, which is used in this study. The temperatures are measured hourly and are provided as daily averages. The accuracy of the measurements is described to be better than 0.04°C (Romanovsky et al., 2008). In addition to that, at some of the sites snow depths were measured in 1-hour time-steps as well. In some parts of the time series, the in-situ measurements show erroneous measurements, what shrinks the available datasets for comparison. To avoid these measurements affecting the general statistics, I calculated monthly averages in order to dismiss those months from the time-series that de- or exceed the monthly average by $\pm$ 10K (cf. Fig. A1). Months, where this is the case, were set NA and not considered in average temperatures or comparisons. Without doing this, years containing erroneous measurements (e.g. due to defective instruments) would affect the general view on the annual temperature cycle.

[3]http://permafrost.gi.alaska.edu/sites_map

3.2 MODIS

The "Moderate Resolution Imaging Spectroradiometer" (MODIS) is an instrument aboard the two NASA Earth Observing System (EOS) satellites Terra and Aqua, acquiring data on a global scale in 36 spectral bands at a spatial resolution of 250 to 1000m. Morning and afternoon, respectively, equatorial crossing-times (Rittger et al., 2013) lead to two different measurement-times per day opening the opportu-

Table 1. Observational site description.

Site	Coordinates Lat, Lon	Location	Elevation $m.a.s.l.$	Vegetation	MAAT $°C$	MAGST $°C$
West Dock (WD)	70.37, -148.55	outer Arctic coastal plain, drained lake basins	3	wet graminoid-moss tundra	-10.1	-7.7
Deadhorse (DH)	70.16, -148.47	outer Arctic coastal plain	17	graminoid-moss tundra, prostrate-dwarf-shrub, moss tundra	-10.1	-3.7
Franklin Bluffs (FB)	69.67, -148.72	inner coastal plain with river terraces	88	graminoid-moss tundra and graminoid, prostrate-dwarf-shrub, moss tundra	-10.6	-3.9
Sagwon (SMAT)	69.43 -148.7	foothills, flat hill crest	278	moist acidic tundra	NA^a	-3.6
Happy Valley (HV)	69.15 -148.84	unglaciated foothills	309	tussock-graminoid, dwarf-shrub tundra and low-shrub tundra	-9.2	-1.8

[a] Air temperatures in Sagwon are missing.

Figure 2. Average annual cycle of Tair and GST. This chart displays the annual cycle in air temperatures (red) and ground surface temperatures (blue) in Deadhorse over the period 2003-2016. Between the darkgreen lines the average snow-free season is displayed, whereas the lightgreen line marks the snowmelt onset day of year. The insulating effect of snow cover is easily recognizable during the winter months. In spring, Tair and GST level up over a longer period than they diverge in autumn. In addition to that, the graph shows a quite high temperature amplitude during the year even though Deadhorse is rather characterized by a maritime than by a continental climate.

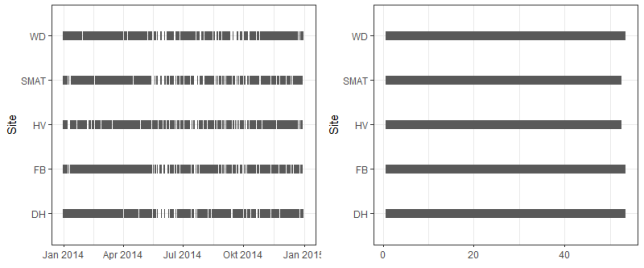

Figure 3. Data availability of MODIS LST. The left figure shows an example year of available land-surface temperatures per day after aggregation of Aqua and Terra satellites but before rejecting low-quality measurements. On the right it is the same year but summarised to weekly values.

nity of two different synoptic situations or even daylight and darkness. The current version 6 datasets are available from early 2000 (Terra) and mid 2002 (Aqua), respectively. All datasets provided by MODIS come in Hierarchical Data Format (HDF) and are gridded using the MODIS Sinusoidal Tile Grid, where every tile is labeled with a horizontal (h) and a vertical (v) index. The study area extends into three tiles, h12v01, h12v02, and h13v01. The three datasets that are utilized on remote sensing basis are LST, NDSI snow cover, and the albedo.

3.2.1 MODIS LST

The version 6 products MOD11A1 (Wan et al., 2015a) and MYD11A1 (Wan et al., 2015b) provide twice-daily per-pixel level 3 LST measurements (thus in principle capturing the diurnal cycle) and emissivity at 1 km spatial resolution. A single tile contains about 1200 by 1200 grids with an exact

grid size of slightly less than 1 by 1 km. The temperature is derived from the 5-minute swath-products MOD11L2 and MYD11L2, respectively. As described in (Wan and Dozier, 1996), the LST retrieval is based on the generalized split-window algorithm from MODIS bands 31 and 32, which is in addition dependent on further parameters such as the viewing angle (Wan, 2014). Wan et al. (2004) report that the target accuracy of single LST measurements is about 1K, however, as this is primarily true for clear-sky conditions (Wan, 1999) significantly reduced accuracies are shown by numerous studies from Arctic regions for individual measurements as well as for hereof derived time-series (Hachem et al., 2009; Westermann et al., 2011). The Scientific Data Set (SDS) in the MOD11A1 and MYD11A1 products include among the LST a set of quality control which can be used to determine the quality of every single measured pixel and eliminate these with insufficient quality[4]. The earlier mentioned uncertainties arising in MODIS measurements in high Arctic latitudes make it necessary to determine to what extent accuracy-loss is acceptable in comparison to the frequency of usable values. Since solely choosing best quality LST would lead to a massive amount of data loss over the study period, pixels with emissivity errors between 0.01 and 0.02 but an LST error equal or less than 1K as well as pixels with an LST error between 2 and 3K but an emissivity error equal or less than 0.01 were not masked and therefore judged acceptable. In the following, the (in the best case) twice-daily satellite-derived LST were aggregated to one daily value for every single pixel, where at least one of four measurements was available. If more than one was available, the resulting LST value is an average. As mentioned before, MODIS measures the earth's land surface temperatures at different daytimes, what might have an effect on the aggregation process due to day- and night-time temperatures. However, Hachem et al. (2012) demonstrate that, in many cases, these values are not related to daylight or darkness, due to the greatly varying diurnal cycle in the high arctic latitudes throughout the year. Based on this, time series of temperature data were created, which still included data gaps from days without any available value. For the compilation of Freezing-Degree-Day (FDD) and Thawing-Degree-Day (TDD) maps an interpolated time series of MODIS-based LST was used so that summation-based measures yield reliable results. For the comparison with observational datasets the data-gap containing but outlier-adjusted time-series were used. Since 2003 was the first year in which both satellites delivered full-year measurements, this was chosen as starting point for the study period.

3.2.2 MODIS NDSI snow cover

The snow datasets utilized in this study are daily L3 global products MOD10A1 and MYD10A1, provided in 500m spatial resolution in the same period as MODIS LST. Snow cover identification is mainly based on the Normalized Difference Snow Index (NDSI), which is a ratio of the difference in visible (MODIS band 4) and short-wave infrared (MODIS band 6) reflectance (Hall and Riggs, 2007):

$$NDSI = ((band4 - band6)/(band4 + band6)) \quad (1)$$

NDSI values greater than 0 are considered as snow cover, whereas values less or equal 0 indicate snow-free land surface. The most effective snow cover detection happens under clear-sky conditions as well as good viewing geometry and solar illumination[5]. Since this is not often prevailing in high latitudes (e.g. cloud coverage, polar night) and the certainty that snow cover indeed has an NDSI value greater than 0 but at the same time, not every NDSI greater than 0 de facto is snow, eight screens are applied to snow detections. These screens are stored in quality assessment flags, which are part of the MOD/MYD10A1 SDS. The value of NDSI snow cover ranges from 0 to 100 and reveals the percentage of the pixel that is covered with snow. That means, the MODIS-based snow data does not provide a snow depth in principle but useful information such as the length of snow coverage can be derived. Alike MODIS LSTs the NDSI snow cover datasets demonstrate reduced accuracies, for instance, due to extended cloudiness. That issue is substantial when start- and end-dates of snow-coverage are derived from MODIS, since several studies demonstrated that, especially in the snow-melt period, a snow-offset delay of a few days can have strong impacts on the ground surface temperature and the surrounding environment (Ling and Zhang, 2003). Dependent on the direction of delay this can lead to longer periods with reduced albedo or altered vegetation periods.

3.2.3 MODIS albedo

The MCD43A3 level 3 albedo product from MODIS (version 6) is a combination of both satellites Terra and Aqua, respectively, provided as daily 16-day product. This bears the opportunity to choose the best observation out of several measurements. The product is provided on daily basis at 500m spatial resolution. For the implementation into the SEB-scheme it was necessary to interpolate the albedo values to 1-hourly (ERA-5) and 3-hourly (ERA-Interim) values, respectively.

[4] https://icess.eri.ucsb.edu/modis/LstUsrGuide/usrguide_1dtil.html

[5] https://nsidc.org/sites/nsidc.org/files/files/MODIS-snow-user-guide-C6.pdf

3.3 ERA reanalysis

The European Centre for Medium-Range Weather Forecast (ECMWF) provides several global atmospheric reanalysis products and two of them are utilized in this study. ERA-Interim as well as the latest product ERA-5 provide global datasets of meteorological variables, based on an assimilation scheme that includes numerous meteorological surface observations (Dee et al., 2011). The gridded surface datasets used from reanalysis products encompass radiation datasets, fluxes, air and dew point temperatures, surface pressure and snow-measures such as snow-melt and snow depth. In addition to that, the elevation of the single ERA-cells was necessary to perform elevation corrections on air temperatures and air pressures, based on actual heights from a 300m resolution DGM. This has been performed with the method similar to (Gao et al., 2012)

$$T_{cor} = T_{ref} + \Gamma \cdot \Delta h \tag{2}$$

where the initial temperature (T_{ref}) is from the ERA-product and lapse rate Γ is set to a fix value of -6.5K per 1km. The difference in elevation (Δh) stems from the ERA-based height and DGM height. Especially the high temporal resolution and the continuous availability of every used variable offer great opportunities for the SEB-scheme used within this study.

3.3.1 ERA-Interim

The global atmospheric reanalysis product ERA-Interim was initiated in 2006 covering the period from 1 January 1979 onwards and provides a comprehensive set of surface variables with approx. 80km spatial resolution (Dee et al., 2011). The sequential data assimilation scheme implemented in the ERA-Interim reanalysis utilizes available observations to produce a coherent record of the global atmospheric evolution. As mentioned before, the archive contains many surface parameters in 3-hourly resolution, as well as 6-hourly analysis meteorological datasets. The ERA-Interim datasets are freely downloadable from the ECMWF's website[6].

3.3.2 ERA-5

In late 2017 ECMWF published the latest reanalysis product ERA-5, firstly for the time-period from 2010 till 2016. Within the working process on this study two more years were published, but these two years are not considered in this study. ERA-5 is a global product with datasets in a much higher spatial resolution (about 31km), providing analysis and forecasting fields in higher temporal resolution as well (1-hour). Among the one high resolution realization (HRES) it contains a ten-member ensemble with reduced resolution. More information on the ERA-5 data can be found on the ECWMF website[7].

4 Methods

A surface-energy-balance scheme was applied to derive the amount of energy that was potentially available for melting snow in a timeframe predefined by both ERA reanalysis and MODIS. In addition to this, MODIS LST was compared to observational datasets to demonstrate its capability of representing air temperatures in high spatial resolution and to map climatic conditions in the study area, providing information on possible differences in thermal conditions. The targeted objective was to create a solid measure of snow-amount at a comparably high spatial and temporal resolution from distance. Since MODIS only provides the time scale of snow events such as snow-on- and offset, an approach was developed and tested, which combines these remotely-sensed measurements with reanalysis data. That means, this scheme reveals high-resolution SWE data sets which cannot be directly measured by satellites as such and which do not require ground measurements (despite of those serving for ERA reanalysis input).

4.1 SEB-scheme

The SEB-scheme utilizes several surface prognostic variables from ERA reanalysis, particularly radiation and turbulent fluxes as well as air temperature, surface pressure, wind speed, relative humidity and a product called snowmelt (provided in mSWE). The idea is, that when every component of the surface-energy-balance is available, solving it for the melt-flux reveals the amount of energy available for melting snow. Which, in turn, gives the opportunity to retrospectively build a snowpack in mSWE over the entire melt-period. As mentioned before, snowmelt comes as mSWE and must be translated into a flux in W/m² using

$$Qmelt_{era} = (Qmelt_{era} \cdot 1000 \cdot L_{fus})/3600 \tag{3}$$

with the latent heat of fusion (L_{fus}). The first step within the workflow was to define the exact start-date of the snowmelt period. This is of great importance, because the approach is based on a logical conclusion: it is only as much snowmelt possible as snow is existing. Thus a segmented linear model is implemented so that those time steps where the linear relation between the accumulated snowmelt and the time is highest are returned as break-points which serve as time limits. This strategy on the one hand tolerates eliminating a few time steps at the beginning of the snowmelt period, on the other hand this prevents the scheme from highly overestimating the melt energy. While the start of melt-period

[6] http://apps.ecmwf.int/datasets/data/interim-full-daily/levtype=sfc/

[7] https://software.ecmwf.int/wiki/display/CKB/ERA5+data+documentation

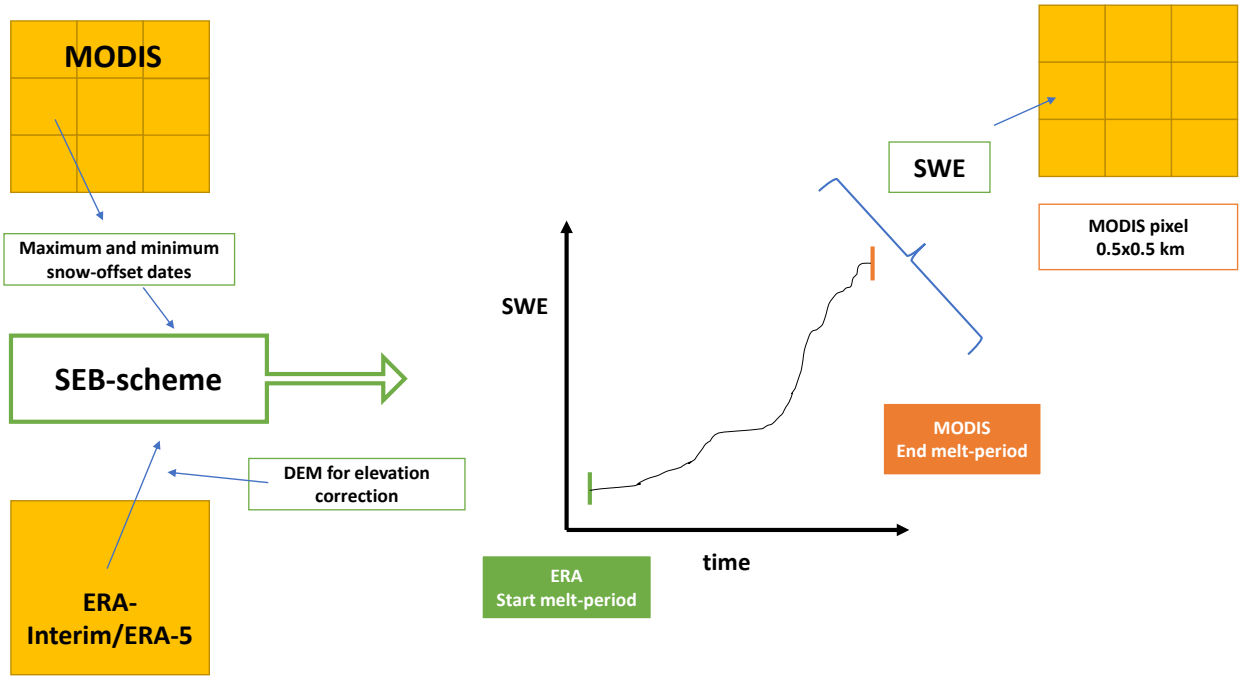

Figure 4. Schematic illustration of the SEB-scheme. The input basis comes from both products MODIS and ERA reanalysis. While MODIS snow-offset dates have to be corrected due to gaps in the data availability, an elevation correction is conducted for surface variables from ERA-5 and ERA-Interim, respectively. These information drive the SEB-scheme which calculates the amount of energy available for melting snow for in a predefined time, which is individual for every pixel. Resulting from this is a SWE value in 500m spatial resolution.

is provided by reanalysis the end-date is derived from remote sensing. This end-date is synonymous with the first day where a NDSI snow cover of 0 was observed. Among the variables provided by MODIS and ERA, numerous surface parameters are implemented in the scheme. Table A1 gives an overview. Both the snow-offset and the albedo value for every individual pixel are satellite-derived and therefore in high spatial resolution. Now, the scheme is applied and computes a melt-term for every pixel. The sensible (QH) and latent heat flux (QE) as part of the SEB are calculated as follows

$$Q_H = -\rho c_p C_h k^2 [\ln(z/z_0)]^{-2} u(\Theta_a - \Theta_s) \tag{4}$$

$$Q_E = -\rho L C_e k^2 [\ln(z/z_0)]^{-2} u(q_a - q_s) \tag{5}$$

where

$$C_h = (1 - 58Ri)^{0.25} \text{ for } Ri < 0 \tag{6}$$

$$C_h = (1 + 7Ri)^{-0.1} \text{ for } Ri > 0 \tag{7}$$

$$C_e = 0.5 \cdot C_h \tag{8}$$

and

$$Ri = gz(\Theta_a - \Theta_s)(\Theta_a u^2)^{-1} \tag{9}$$

represents the Bulk-Richardson number acting as stability criterion (Kustas et al., 1994). ρ represents the density of air, specific heat of air at constant pressure is represented by c_p, k is van Karman's constant, u displays wind speed and L is the latent heat of vaporization. The gradients are represented by height z and roughness length z_0, by the potential temperature at height z, Θ_a (where a stands for air) and at the surface Θ_s, as well as the specific humidity q_a and q_s, respectively. The surface temperature is set to constant 0°C, firstly because the surface is expected to be near the melting point during the melt period, which is, secondly, the time of the year significant for this study. In addition to that, I only account for a positive melt flux, meaning that snow ablation is the exclusive event interesting for this study's means. Snow-accumulation is neglected within the SEB-scheme and since temperatures below 0°C would lead to deposition, this process is excluded by setting the surface temperature to 0°C.

The Thornthwaite-Holzman Bulk transfer approach, which is used here, is based on a couple of simplifying assumptions (Kustas et al., 1994). This includes the application of similar roughness lengths for water vapor, heat as well as momentum, and simplified stability corrections, represented by Ch and Ce, respectively, where Ch is suggested to be about the same as the momentum transfer and Ce is approximately half of it (Morris, 1989). Now

$$Qmelt = Q_{net} + Q_H + Q_E - Q_G \tag{10}$$

with

$$Q_{net} = SW_{in}(1 - albedo) + \epsilon LW_{in} - LW_{out} \tag{11}$$

is used to measure the flux of energy which is available for melting snow. In Eq. 10 net radiation is a combination of reanalysis products (SW_{in} and LW_{in}), the MODIS derived albedo and an outgoing longwave radiation at the constant surface temperature of 0°C based on the Stefan-Boltzmann-law

$$LW_{out} = \epsilon \sigma T_{surf}^4 \tag{12}$$

where ϵ is emissivity of the surface (here melting snow), σ is the Stefan-Boltzman's constant and the absolute temperature (in K) at the surface T_{surf}. Resulting from this workflow a MODIS-pixel-based potential amount of snow (in SWE) that could have been melted throughout the period is derived in 500m spatial resolution based on snow-input of sub-daily resolution.

4.2 SEB-scheme part 2 - requirements

The combination of two data sources that come in different spatial and temporal resolution leads to several issues which must be negotiated. In this section requirements are described that were inevitable for a smooth run and a satisfactory model outcome.

4.2.1 Ground heat flux

The generation of the melt-flux in this approach is based on solving the SEB (Eq. 10). Turbulent fluxes are calculated within the scheme and net radiation is derived from the input datasets. ERA-Interim does not provide a ground heat flux (QG), thus, this parameter has to be determined in advance. That happens in a similar way like the scheme operates, but with a slightly different set of input variables. In this case, QH and QE as well as Q_{net} are solely derived from reanalysis data since the snowmelt calculation is also calculated as a function of these parameters (among others). Here, it is necessary to act as close to ERA as possible in order to calculate the most convenient guess of ground heat flux related to the other input variables of ERA. The ground heat flux is then calculated as follows

$$QG = Q_{net} + QH + QE - Qmelt \tag{13}$$

where the radiation balance is

$$Q_{net} = SW_{net} + LW_{net} \tag{14}$$

with reanalysis-based SW_{net} and LW_{net} as mentioned before. For the application of the basic SEB-scheme both a fix QG fraction (based on the median value over the melt-period) and the altering value were tested for ERA-Interim and ERA5, respectively.

4.2.2 Land-sea-fraction

A different issue arises within the workflow, which is due to ERA reanalysis' coarse spatial resolution. The northern part of the study area is located next to the coast, thus inevitably leading to water-containing grids. The problem is that the snowmelt product suffers from the water fraction and gives different values than those where only land surface is embedded. To avoid this, for every ERA-grid-cell where water is included, the snowmelt value is imported from the southward neighboring cell whereas all other values remain from the initial cell.

4.2.3 MODIS data gaps

As outlined in Section 3.2, MODIS datasets especially in the high latitudes suffer from large data gaps. Since MODIS snow-offset dates serve as time limit for the melt-period, these outages can have a crucial impact on the resulting melt energy. Treating the first day on which MODIS detects 0 NDSI snow cover as fix snow-offset date may lead to misrepresentations due to possible days without any available detection between the first 0 and the last measured snow cover. To address this, the SEB-scheme is run twice, once with minimum snow-offset and then with maximum snow offset. After that, a mean value is calculated and treated as best guess between the two extremes.

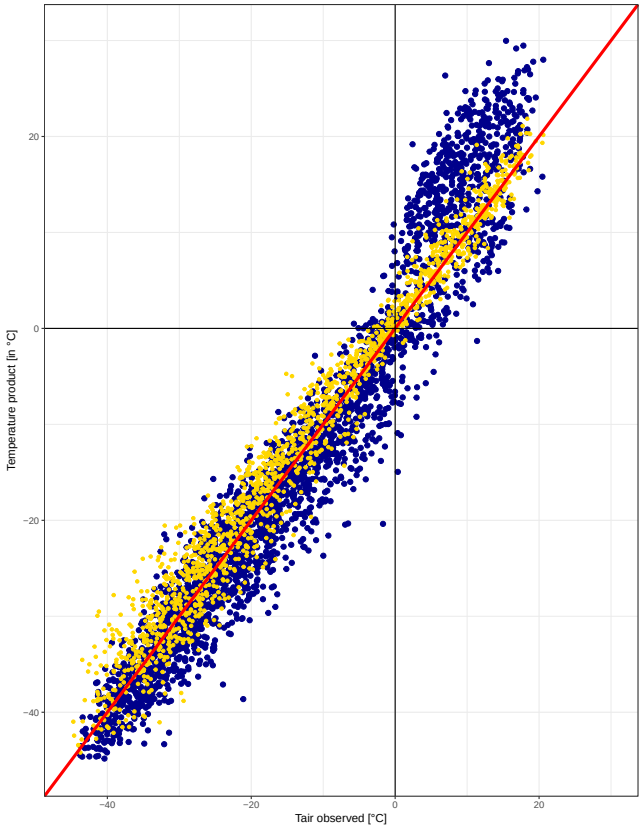

Figure 5. Scatterplot MODIS/ERA and measured Tair. The graph shows the comparison of MODIS LSTs as well as ERA5 air temperatures and observed temperatures (MODIS in blue and ERA5 in yellow, respectively) at the Franklin Bluffs site on a daily basis. It is displayed that MODIS slightly underrepresents the LST when temperatures are below 0°C and overestimates them in the summer season. ERA-5 indicates an opposing pattern for the cold time of the year as well as a good fit in summer.

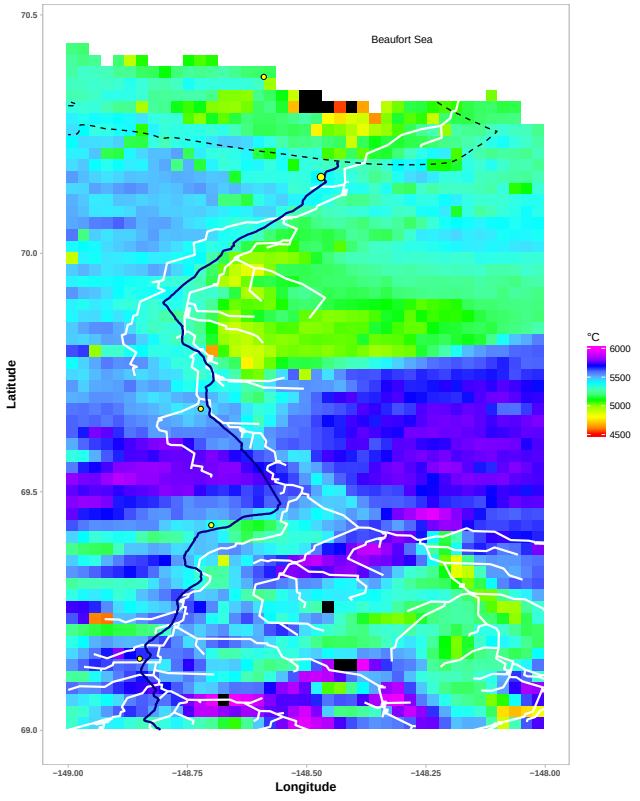

Figure 6. Average Freezing-Degree-Days. This graph shows the average FDD over the ERA-5-covered time series 2010-2016. FDD are the sum of daily temperatures below zero and are displayed as absolute value, meaning the highest value equals the coldest temperatures. The Saganavirktok River is displayed in white, the Dalton Hwy in blue and the five validation sites are marked in yellow, with Deadhorse/Prudhoe Bay being emphasized. The black dotted line encompasses the Prudhoe Bay Oilfield. Highest FDD values are displayed in the flat regions in the center of the study area, whereas the hill north of that shows comparably low FDD.

5 Results

5.1 Validation of the forcing datasets

Since MODIS LST and snow data sets are utilized for detecting the permafrosts thermal state, it was of great importance to see how the observed temperatures in the study area are represented by MODIS. In a first step, MODIS LST measurements were compared to observed GSTs and air temperatures to get an overview of the single relations and representations. Several studies suggest concentrating on observed air temperatures, because these are much better represented by MODIS LST. Since MODIS-based measurement of LST is strongly influenced by surface conditions, these temperatures reveal a great insight in the near-surface temperatures and therefore the thermal regime of the surface. But, to address the thermal state of the ground, it is necessary to have more snow data in detail even though snow cover might be quite shallow. The mismatch between GST and LST (cf. Fig. A3) is easily recognizable, whereas daily air temperatures available at four of the five validation sites are well represented with an average R = 0.95. Furthermore, MODIS underestimates the observed air temperatures, primarily in the cold section of the year (cf. Fig. 5), which is well represented by negative MBE at all validation sites, especially during the months October till May. Overall, MODIS-derived LSTs deviate about ± 5K for daily observed temperatures and about ± 4.5K for weekly averages. On the contrary to the underestimation of cold-season temperatures, those in the predominantly snow-free season between June and September are constantly overestimated. ERA reanalysis also reveals errors in estimation, however, the reanalysis product (ERA-5 displayed in Fig. 5) overestimates the overall temperatures, with a variation of about ± 3K around the daily values. Concern-

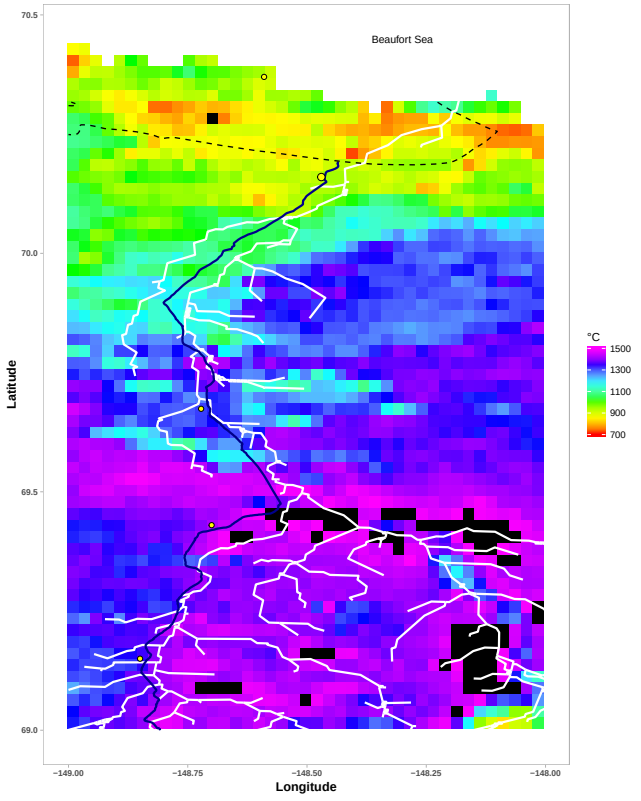

Figure 7. Average Thawing-Degree-Days. This graph shows the average TDD over the ERA-5-covered time series 2010-2016. Opposing to the FDD, TDD are the sum of daily temperatures above zero. The highest values cover the areas southward of the coastal region, with peak TDD in similar regions as FDD. Some pixels exceeding TDD=1500°C were masked (black pixels) in order to maintain a certain spatial diversity.

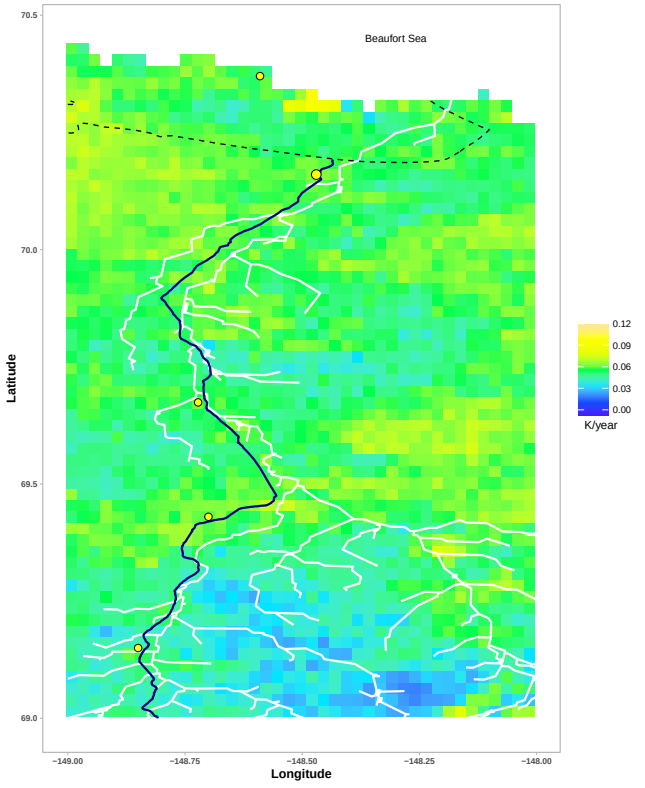

Figure 8. Annual trend in MODIS LST over the period from 2003-2016. The temperature trend is based on weekly averages of MODIS LST. The entire study area reveals a warming trend, no pixel has been detected with a decrease or stand-still condition. The strongest increase is up to 0.1K per year, the overall range is displayed from darkblue (smooth) to orange (strong).

ing MODIS' snow-on and -offset usability, most of the pixels show a meltperiod length between 5 and 20 days (cf. Fig. 12), depending on their location. The average meltperiod length over the entire study area is about 17 days and therefore only little longer than reported by Stuefer et al. (2012). That means, despite of its reduced accuracy, MODIS is able to provide useful information on the snow cover and especially on the snowmelt period.

5.2 Climate Monitoring based on MODIS

In Figure 6, FDD for the whole study area are shown for a sample year. Some topographic features of the study site such as the slightly more elevated region in the center of the study area reveal lower FDD. Furthermore, the exposed hillsides of the Brooks Range or the coastal zone are easily recognizable, as these exhibit lower FDD than the surrounding areas. The flatter areas show higher FDD throughout the year. In addition to that, some interesting features show up near the coast, where some isolated pixels show quite large differences compared to the neighboring ones. The Saganavirktok River does not show different FDD than the adjacent areas, despite of the valleys in the foothills of the Brooks Range. Both average FDD and TDD over the entire study period highlight the maritime and continental climate's, respectively, influence. The largest amplitude is found in the center of the study area, whereas the coastal zone is characterized by a lower amplitude. Trend in air temperatures derived from MODIS (cf. Figure 8) over the entire period reveal a warming for every pixel in the study area with maximum increases of up to 0.1K per year. Similar to the FDD-map, Figure 8 shows the strongest warming trend over the years especially in the flatter, colder areas in the center of the study site as well as next to the coast. Slower warming trends are shown in the elevated center and primarily in some parts of the Brooks Range. This demonstrates that the temperatures in colder regions experience are stronger warming trend than comparably warmer areas. Despite of this muster, some adjacent pixels reveal a very large difference in warming trend. For instance, pixels in the coastal area, where numerous ponds and lakes can be

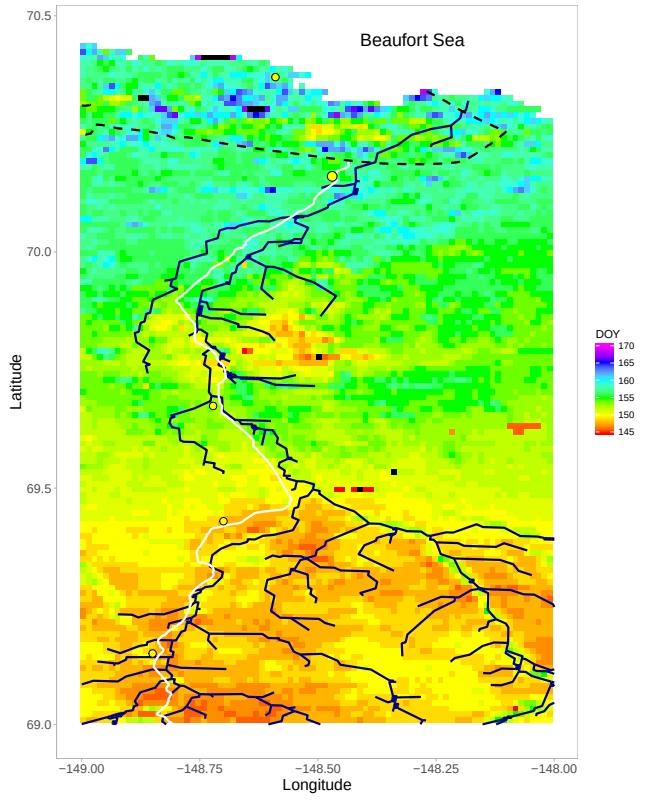

Figure 9. Snow-offset DOY on average over the 14-year period from 2003 to 2016. This is an average value that is based on the mean value of the last day where MODIS discovered snow in each pixel and the na-corrected value. In this context, snow-coverage means any NDSI other than 0 per pixel. The snow-offset date is the first day where no snow-cover was detected. Among the increasing snow-offset date gradient from soth to north the map reveals some topographical features typical for the study area. For instance, the elevated center is sooner snow-offset than surrounding areas.

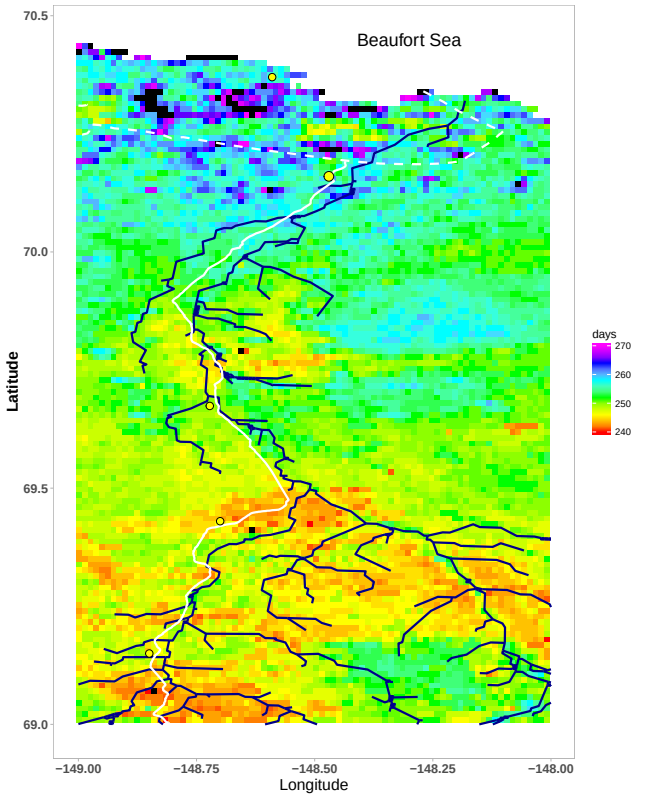

Figure 10. Average length of snow cover season during 2003-2016. The amount of snow-covered days (solely based on MODIS) per year varies significantly within the study area. Generally, the length of the melt period decreases from north to south.

found, show differences of 0.05K per year. Regarding the observation sites, the highest overall value was calculated for Deadhorse (0.9K), closely followed by Franklin Bluffs and Sagwon (0.8K). The smallest trend was found for Happy Valley (0.6K) at the foothills of the Brooks Range. For the 18-year-period from 1986 to 2003 Osterkamp (2005) found similar warming trends for Deadhorse and Franklin Bluffs, also with the higher values in Deadhorse. Figure 16 displays emerging patterns in average snow-offset date based on MODIS in the study area. From North to South the snow-offset date decreases with maximum differences of about 20 days. This is also reflected by the closest pixels to each of the study sites, resulting in a 9-day difference between West Dock and Happy Valley representing the northernmost and the southernmost observation site, respectively. Nonetheless, especially in the southern part, some opposing patterns were detected such as next to the Saganavirktok River, which is emphasized by comparatively late offset-days, whereas some pixels next to the Beaufort Sea present early offset-days in comparison to the surrounding pixels. However, several pixels revealing a later snow-offset make the coastal area to a very diverse region concerning snow features. In addition to that, the average snow season length (Figure 10) displays equal patterns for near-mountain pixels and the hilly parts in the center. Here, the snow-covered season is shorter than the study area's average (251 days). Also, alike snow-offset dates, snow-covered seasons tend to be longer along the coast. Despite of again some contrasting pixels that show large differences on very small spatial scale. Over the ERA5-covered period from 2010 till 2016 the complete snow-offset date tends to be earlier for several sample pixels in the entire study area (Figure 16). In addition to that, trends show an earlier snow-offset at the end of the study period (averaging about 9 days), especially in the northern half of the study period (cf. Fig. A4).

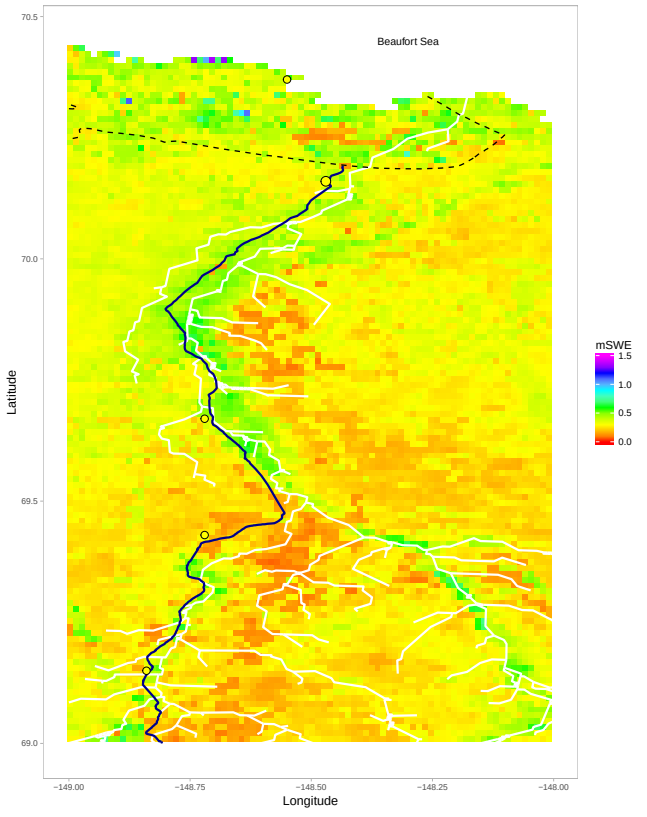

Figure 11. peak-SWE in the study area in 2013 based on MODIS and ERA5. This figure shows mean peak-SWE values calculated from the minimum and maximum SWE results for the sample year 2013. The indicated value is the maximum SWE that could have been melted throughout this snow-melt season. The map clearly displays the Saganavirktok River and some of its distributeries. In addition to that, especially in the elevated region in the center of the study site the SWE values are small. Several pixels next to the coast are characterized by similar values as the pixels adjacent to the river.

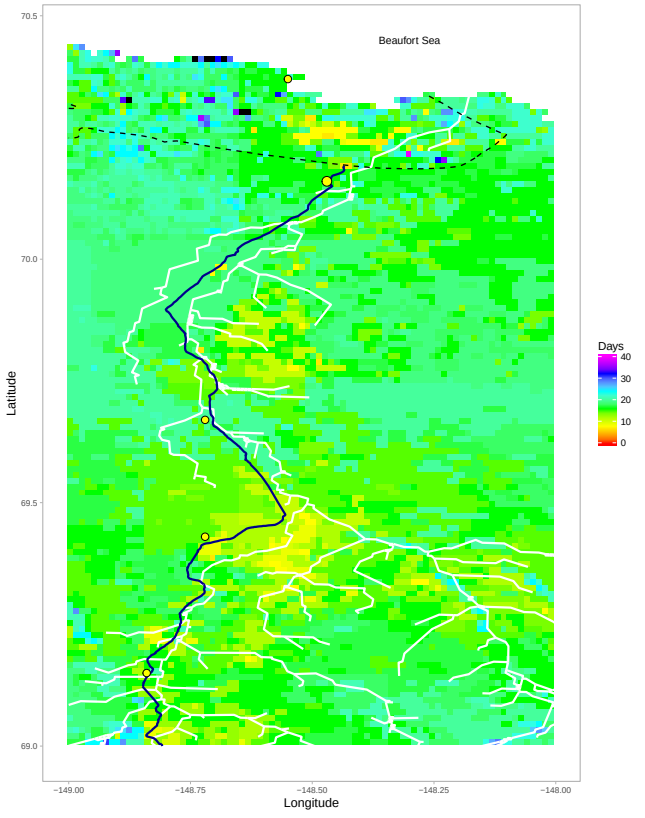

Figure 12. Length of meltperiod in 2013. The graph displays the meltperiod lengths derived from from MODIS (showing the average between minimum and maximum) for the year 2013. Most of the pixels are snow-free in less than three weeks.

Table 2. ERA-5-based average peak-SWE and melt period length.

Site	mSWE	Melt period
WD	0.74	27 days
DH	0.4	19 days
FB	0.4	21 days
SMAT	0.25	16 days
HV	0.29	16 days

5.3 Model performance

Figure 11 displays the modeled peak-SWE values for the sample year 2013. It shows that the scheme is able to provide feasible results concerning the maximum amount of SWE that could have been melted. Especially, some topographical features are displayed quite well in the map. Pixels next to the Saganavirktok River and its channels reveal comparably high SWE values. In addition to that, the coastal area where numerous ponds and lakes occur, is on the one hand often represented by high SWE values. On the other hand, several pixels exist that display comparably small SWE values. As represented by the black dotted line in the map, this is exactly the Prudhoe Bay oil extraction area, which might be an influencing factor. It is likely to see, that especially on the north-western side of the hill in the center the SWE values are large. Here it seems like the exposition strengthens the effect of the river course. Generally, the SWE-map displays that SWE values can differ greatly on a small spatial scale. Comparisons between the years show that snow patterns differ greatly, besides of recurring patterns that are often related to topographical features, and change over the years. According to measurements in the study area (Romanovsky et al., 2008) the SEB-scheme overestimates the amount of snow that could have been melted. An average annual peak-SWE of 0.31 over the ERA-5-covered period from 2010-2016 equals about 1m snow depth, depending on the snow density. This finding is accompanied by an overrepre-

sentation of the meltperiod (cf. Fig. **??**), which has a direct influence on the amount of SWE that is calculated by the SEB-scheme. Furthermore, Stuefer et al. (2012) report on a net decrease in SWE from north to south which is also represented by the SEB-scheme, displayed in Figure 11. Concerning the single observation sites, the longest snowmelt period was calculated for the northernmost site, West Dock, as well as the shortest for both sites at the foothills of the Brooks Range (cf. Tab. 2). The SEB-scheme reveals a decrease in meltperiod length from the northern to the southern part of the study area. This gradient is also reported by Stuefer et al. (2012). Figure 14 displays, that both ERA-5 and ERA-Interim are able to present feasible SWE results. However, the coarse resolution of ERA-Interim is easily recognizable in the coastal areas with an abruptly weakening representation of SWE values. The spatial diversity of SWE within this study area is what leads to large uncertainties in monitoring permafrost's thermal state and active layer thickness. Increasing near-surface temperatures, especially in the coldest regions of the study area (cf. Fig. A4), and an earlier snowmelt in spring, lead to an enhanced warming of permafrost temperatures.

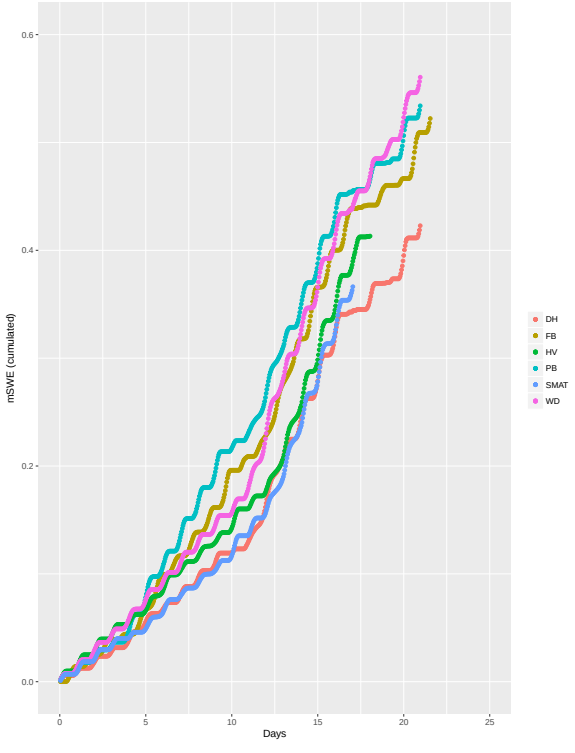

Figure 13. Melt period in 2013 in the SEB-scheme. Here, the melt period is defined by ERA reanalysis and by MODIS. The meltperiod length calculated within the SEB-scheme equals about three weeks which ends up with a similar melt period length as measured by MODIS. It is shown that the two southernmost observation sites have shorter melt periods than the sites in the northern part of the region.

6 Discussion

6.1 MODIS perfomance

Over the entire study period MODIS appears to be a useful tool for estimating LSTs on a large spatial scale in the high Arctic. The overall characteristics of the climatic patterns match those values derived from the observation sites. MODIS-derived FDD- and TDD-maps display topographic and climatic differences in the study area as well as the derived trends towards warming temperatures are similar to long-term ground-based measurements (Romanovsky et al., 2008). However, some implications arising from satellite-based monitoring of surface parameters cause occasionally erroneous measurements or require assumptions which deteriorate the quality of MODIS-based measurements. Though pixels detected as cloud are automatically rejected by an included cloud mask, not all clouds are identified as such leading to cloud top temperatures within the MODIS-derived LST (Westermann et al., 2015). This cloud-detecting mechanism was found to be imperfect especially during dark conditions (Liu et al., 2004) what applies for the entire polar night season. Figure 5 shows that phenomenon also appearing for the observation site in Franklin Bluffs representative for the study area. Over an entire year, MODIS slightly underrepresents the temperatures.

6.2 Applicability of the forcing data

Very important for the performance of the SEB-scheme is the determination of the melt period. Figure 15 displays the meltperiod metrics for the sample year 2012. It displays the high spatial variation of snowmelt throughout the study area, however, the start date is quite consistent. Stuefer et al 2012 state that within a study in 2011 and 2012 the onset of snowmelt at numerous sites in the study area happened around mid-May, which is consistent with the reanalysis-based snowmelt-onset. The MODIS-derived end of snowmelt also matches the reported early-June complete snowmelt. Figure 5 shows that the air temperature from ERA-5 depict the observed value quite well. The spatial and temporal differences of the two forcing datasets makes implementing a few simplifications necessary which could potentially bear uncertainties. A remarkable source of uncertainty can be the MODIS-based snow-offset date due to the large data gaps between the first DOY with 0 NDSI and the last DOY where any snow-cover has been measured. For some pixels this gap can extend to more than 20 days what has a tremendous impact on the potential amount of SWE. For the final maps the average value between these two has been chosen to be the best guess. Further issues arise due to the different temporal and spatial resolutions of the two datasets. For instance, ERA-5 and ERA-Interim provide hourly and 3-hourly, respectively, values for snowmelt and snow depths, respectively, whereas MODIS comes up with measurements on a

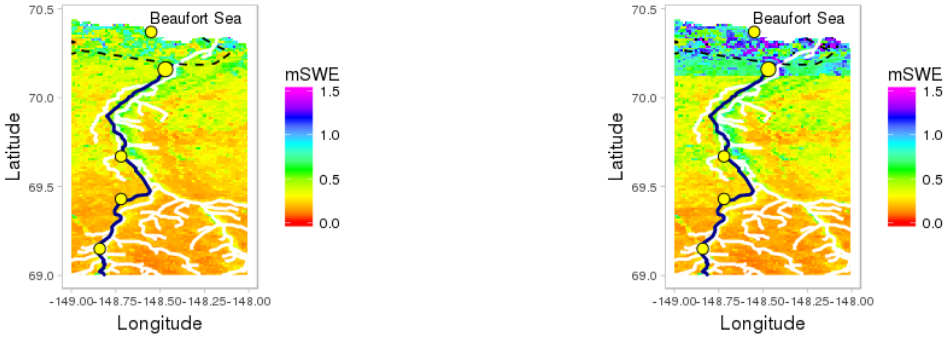

Figure 14. Comparison of ERA5 and ERA-Interim. These two maps show the SEB-scheme's performance based on ERA-Interim (left) and based on ERA5 (right), respectively, in 2011. Both products show very similar patterns, especially from Deadhorse southward. However, primarily at the coast ERA-Interim based SWE values escalate. The overall distribution of larger and smaller SWE values is very similar, but in a different order of magnitude. Despite of that, the great difference in spatial resolution is not recognizable while concentrating on the southern part of the study area.

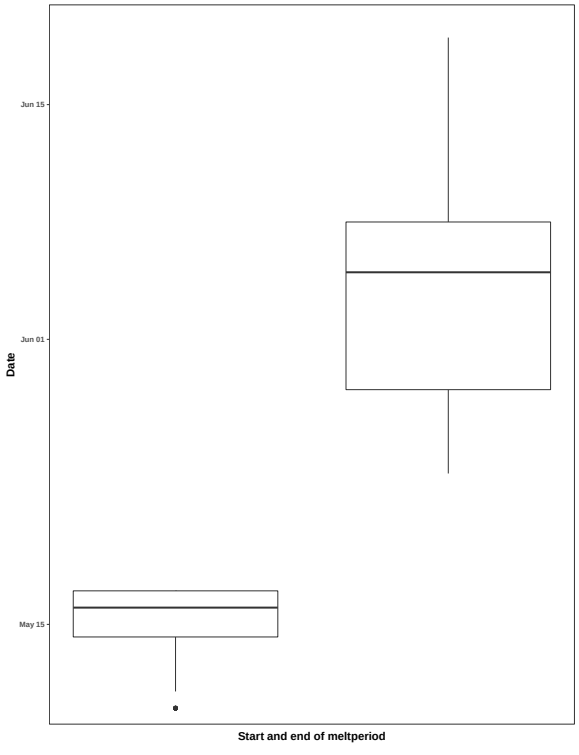

Figure 15. Meltperiod metrics. This graph shows the start (left) and end dates (right) of the meltperiod for a number of pixels evenly distributed in the study area from 2012. This date is derived from ERA-5 by the means of a segmented linear model. The meltperiod starts for most of the pixels by mid-May and ends for most of the pixels within the first days of June. The start of meltperiod is displayed with much less variation than the end date.

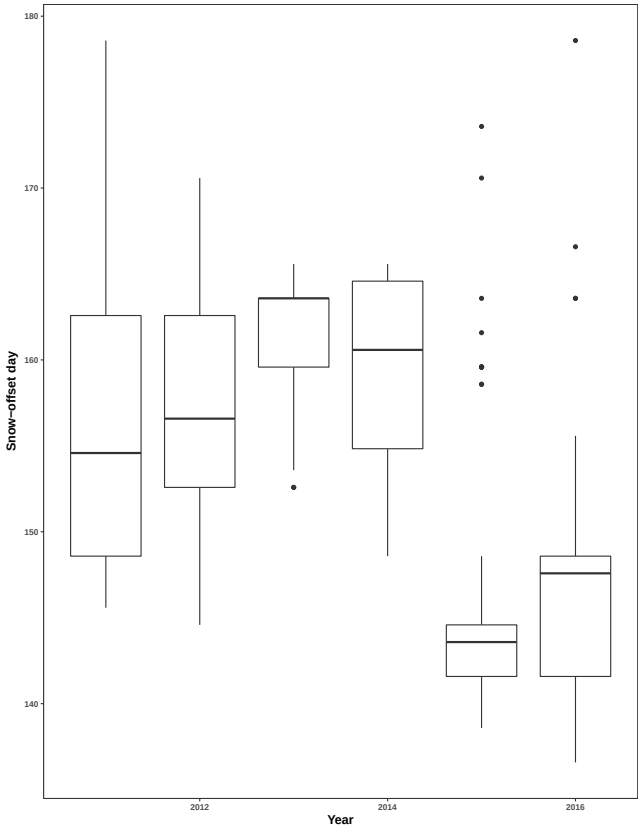

Figure 16. MODIS snow-offset over the years. The comparison of these snow-offset dates show a trend to earlier complete snow-offset. In addition to that, the variation between the years reveals differences, but primarily the spatial distribution within a year is quite large.

daily scale. Therefore, the remotely-sensed snow-offset DOY has to be interpolated to at least 3-hourly time-steps, leading again to uncertainty concerning the true sub-daily end-point. For instance, a MODIS-based end-DOY 160 bears the opportunity of 24 time-steps on the reanalysis time-scale which influences the SEB-scheme. As explained before, both ERA-5

and ERA-Interim grid cells near the coast contain water fractions. Since this influences the reanalysis-derived snowmelt term, it is loaded from the neighbouring cell in southward direction. On the one hand, this is a feasible mechanism in order to derive a suitable start-date of the meltperiod. On the other hand, implementing a different grid cell's melt-term may have an impact on the calculation of QG (cf. Eq. 13), which, in turn, has an impact on the resulting SWE values. This is because the utilized fluxes stem from different calculations. Since ERA-5 grid spacing is much higher than ERA-Interim, the impacts are larger in ERA-Interim-based calculations.

6.3 Performance of the SEB-scheme

Among many uncertainties and issues arising throughout the working process, topographical features such as the Saganavirktok river or elevated areas are detected and present feasible results.

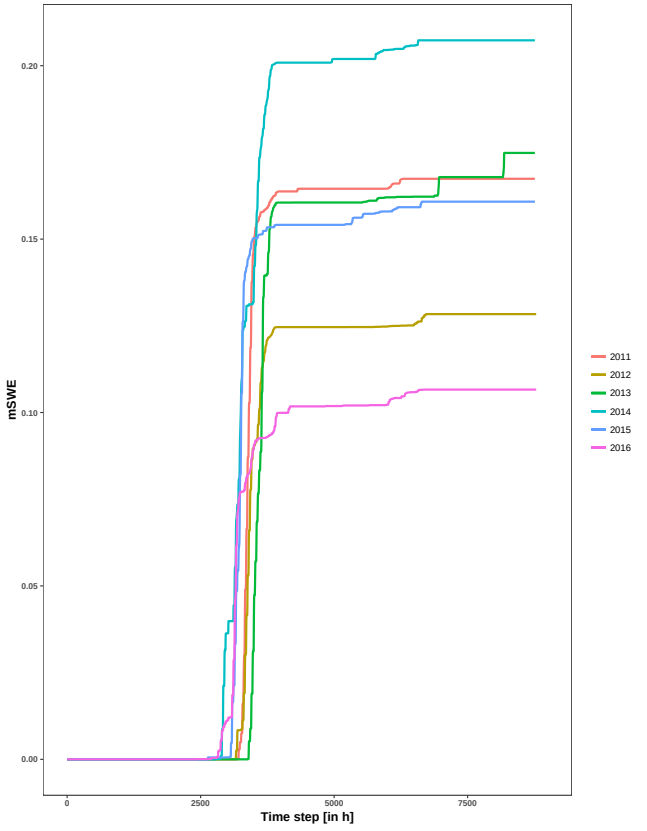

Figure 17. Accumulated snowmelt over the years. This graph shows the accumulated snowmelt from ERA-5 between 2011 and 2016. It is well displayed that the year 2014 has the highest curve whereas 2016 has the smallest. This high amount of accumulated SWE, which is as part of the SEB conterminous with a high amount of melt energy, leads to a high resulting $Qmelt$.

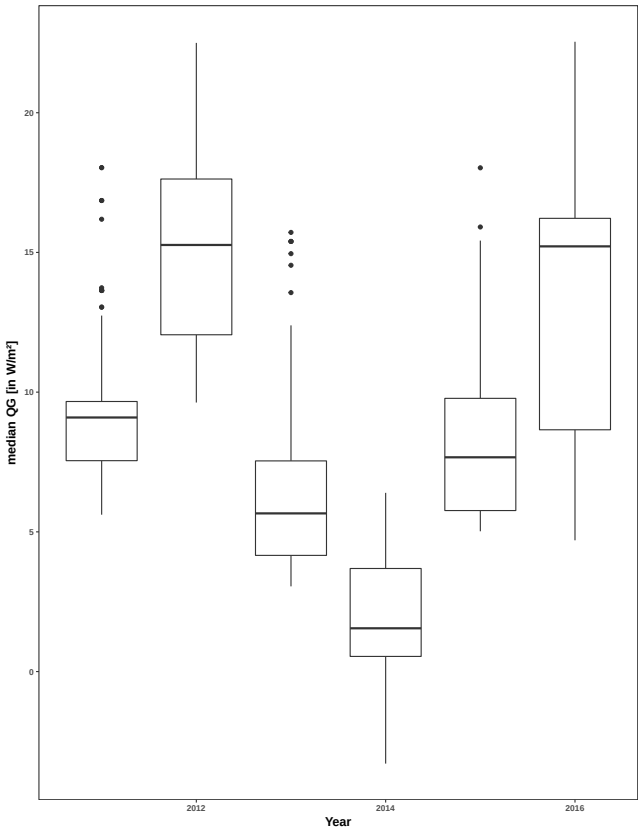

Figure 18. Ground heat flux over the years. This graph shows the value of the ground heat flux calculated within the scheme. Similar to the accumulated SWE value in Figure 17 the lowest median values of QG are calculated in 2014.

The utilization of a segmented linear model for the derivation of ERA-based snow-melt period as simplification of the time of the year where the most significant melt happens, leads to an uncertainty concerning the true initial date of snowmelt and the true end date of snowmelt. This is because the melt-period starts with the first time step revealing the strongest shift in snow-coverage and ends somewhere between the MODIS-derived minimum and maximum value. However, as mentioned in 5.1, this approach seems to yield feasible results compared to observed melt period onset dates. Figure 14 displays that both reanalysis products are able to represent the overall situation, whereas ERA-5 is much more accurate in the coastal regions due to its higher spatial resolution. Furthermore, the SWE maps show quite large differences between single years (Figure A2). During the ERA5-covered period between 2010 and 2016, primarily 2014 shows differing (much larger) SWE values. Larger calculations of SWE values can be based on both a long melt-period and on the forcing data, especially the fluxes and radiation. Figure 16 displays that this finding is not initialized by higher MODIS inaccuracies in this specific year. As it turned out, the critical influencing variable in this case is most

likely snowmelt derived from the reanalysis dataset. Figure 17 shows accumulated snowmelt values for the years 2011 till 2016 with the highest curve representing 2014. Now, this accumulated snowmelt influences the ground heat flux equation (Eq. 13). The higher the snowmelt, the smaller QG (cf. Fig. 18). This, in turn, affects the SEB-scheme's Q_{melt} calculation (Eq. 10). Ultimately a high melt flux in the forcing data leads to a high amount of melt energy calculated by the scheme.

7 Conclusion

MODIS-based climate monitoring reveals a warming trend in the entire study area and its patterns are found to represent observed values quite well. However, some neighboring pixels show quite large differences, primarily in the flat coastal area. At the same time, MODIS provides high resolution information on snow cover which can be implemented in a surface-energy-balance-scheme. The SEB-scheme is capable of using MODIS-derived snow and LST data for downscaling ERA reanalysis by relatively small computational cost. The resulting SWE maps show patterns which were demonstrated by the MODIS climatology. Furthermore, it displays the spatial variability of SWE within the study area, which is the source of large uncertainties in permafrost monitoring. Since ERA-5 datasets for the period from 1950 onwards will be released soon, longer time series can be established. But still, limitations arise due to gaps in MODIS-based snow cover monitoring. Furthermore, for future SWE monitoring, a higher spatial resolution without deterioration of temporal resolution would be desirable in order to address and monitor small-scale snow conditions.

Acknowledgements. I would like to express my gratitude to my supervisor Dr. Moritz Langer for his engagement, valuable comments and numerous ideas through the learning process of this master thesis. Thanks for your great help, for proofreading and for your patience with explaining stuff again and again. Furthermore, I would like to thank Dr. Sebastian Schubert for providing me with plenty memory space, computing capacity and for his patience regarding this. Finally, I would like to thank my friends and, particularly, Nora for their support and encouragement.

Appendix A: SEB-Scheme

This is the SEB-scheme applied over the melt period with both MODIS-based and ERA reanalysis input. In this case the scheme is based on ERA-5 datasets, ERA-Interim requires a slightly different scheme due to differing temporal and spatial resolution.

For every year a file has been prepared in advance which contains information about MODIS-derived albedo (interpolated to temporal resolution of ERA product), the first day of zero NDSI snow cover and the last measured snow cover for every pixel.

```
year = yearofinterest
setwd("/data/scratch/kemperta/MA/SWE/MODIS_files/")
modis_predefined = paste0("modis_combo_era5_",year,".
    csv")
modis_file = read.csv(modis_predefined)
```

The input file also contains information on the coordinates of every pixel which is important in the further steps within the scheme because the different sets of data are joined by their coordinates. For verification means I add an additional column containing the pixels "id". This makes error detection much easier.

```
modis_coordinates = modis_file[,1:2]
modis_file$id = 1:length(modis_file$first_zero)
```

After loading the input file the actual scheme starts. Here, the workflow is conducted for every single MODIS-pixel which is, depending on the year, more than 9000. These pixels are dialed row-wise, so that the current working table contains the respective coordinates, snow-offset DOY, and MODIS-derived albedo. In addition to that, the NA-gap between the last measured snow value unequal zero and the first observation of zero NDSI snow cover is included.

```
for (i in 1:nrow(modis_file)){
data = modis_filef[i,]
mod_coordinates = data[,1:2]
mod_first_zero = data[,6]
mod_last_detection = data[,5]
mod_na_diff = mod_first_zero - mod_last_detection
mod_na_diff = mod_na_diff - 1
marker1 = length(data)
marker2 = marker1 - 1
mod_albedoinfo = data[,c(10:as.numeric(marker2))]
diff = ifelse(is.na(mod_na_diff), mean(modis_file$Diff
    , na.rm = T), mod_na_diff)
diff = ifelse(mod_na_diff < 0, mean(modis_file$Diff,
    na.rm = T), mod_na_diff)
diff = round(diff, digits = 0)
mod_step = data[,marker1]
```

For every MODIS-pixel the overlapping ERA grid cell is loaded by the means of minimum distance between the two products.

```
df_lat = c(70.5, 70.5, 70.5, 70.5, 70.2, 70.2, 70.2,
    70.2, 69.9, 69.9, 69.9, 69.9,
           69.6, 69.6, 69.6, 69.6, 69.3, 69.3, 69.3,
               69.3, 69.0, 69.0, 69.0, 69.0)
df_lon = c(210.9, 211.2, 211.5, 211.8, 210.9, 211.2,
    211.5, 211.8, 210.9, 211.2, 211.5, 211.8,
           210.9, 211.2, 211.5, 211.8, 210.9, 211.2,
               211.5, 211.8, 210.9, 211.2, 211.5,
               211.8)
coords = as.data.frame(rbind(df_lat, df_lon))
t_lat = which.min(abs(mod_coordinates$y - df_lat))
t_lon = which.min(abs(mod_coordinates$x - (df_lon -
    360)))

target_lat = coords[1,t_lat]
target_lon = coords[2,t_lon]

file_era = paste0("era5_",year,"_hourly_",target_lat,"
    _",target_lon,".csv")
setwd("/data/scratch/kemperta/MA/SWE/ERA_files/")
era5 = read.csv(file_era)

era5$initstep = c(1:length(era5$Snowmelt))
```

Since this has been done, the input data is loaded, fixed value are set, and surface variables are calculated.

```
T_z = era5$Tair + 273.15
T_0 = 0
T_0[1:length(era5$Tair)] = 0 + 273.15
Tsurf = T_0 - 273.15
Psurf = era5$Psurf * 100
u_z = era5$wind
R = 287.058
cp = 1005.7
rho = Psurf / (R * T_z)
g = 9.81
z = 2
z0 = 5 * 10^-4
k = 0.4
L = 2501 * 10^3
Lfus = 334 * 10^3
sbk = 5.67 * 10^-8
epsilon = 0.985
Tdew_air = era5$Tdew - 273.15
d2m_s = Tdew_air
RH = era5$RH

e = 6.112 * exp((17.625 * (d2m_a))/(243.04+(d2m_a))) *
    100
q_z = (0.622 * e)/Psurf

Tdew_surface = Tsurf - ((100 - RH)/5.)
Tdew_s = Tdew_surface

e = 6.112 * exp((17.625 \cdot (Tdew_s))/(243.04+(Tdew_
    s))) * 100
q_0 = (0.622 * e)/Psurf
```

In the next step, the net radiation is calculated based on ERA reanalysis input.

```
Qnet_era = era5$SWnet + era5$LWnet
```

Since the ERA-derived variables are implemented, I can address the coastal issue and load the new file, if necessary, without changing the original forcing. If grid cell is not located next to the coast, it is only the original file that is loaded again.

```
neighboring_lat = 70.2
target_lat = ifelse(target_lat == 70.5, neighboring_
    lat, target_lat)
file_era = paste0("era5_",year,"_hourly_",target_lat,"
    _",target_lon,".csv")
setwd("/data/scratch/kemperta/MA/SWE/ERA_files/")
era5_snowmelt = read.csv(file_era)
```

The snowmelt is accumulated and utilized as basis for the segmented linear model. I am interested in the first breakpoint, as this reveals the start-date for the melt period.

```
snowmelt_era_accumulated = cumsum(era5_snowmelt$
    Snowmelt)
era5$acc_smelt = snowmelt_era_accumulated
model.response = era5$acc_smelt
model.predictor = era5$initstep
```

```
try(model.lm = segmented(lm(model.response~model.predictor),
seg.Z=~model.predictor,psi=NA, control = seg.control(K=3)))

df_breakpoints = as.data.frame(model.lm$psi)
first_bp = as.data.frame(round(min(df$Est.)), digits = 0)
bp_1 = as.data.frame(which(era5$initstep %in% first_bp))
names(bp_1) = "bp1"
```

Here, the snowmelt in mSWE is converted to $W \cdot m^-2$.

```
Qmeltterm_era = (era5_snowmelt$Snowmelt * 1000 * Lfus) / 3600
```

While I have the start-date of the melt period, I need to set the end-date by MODIS. Since MODIS provides daily values the end-point needs to be interpolated to hourly time steps coherent with ERA reanalysis.

```
off = as.data.frame(mod_first_zero)
off = off - diff
date_string = paste0(year,"-01-01")
off$Date = as.Date(off$mod_first_zero, origin = date_string)
year_start = paste0(year,"-01-01 00:00:00")
year_end = paste0(year,"-12-31 23:00:00")
date_hourly = as.data.frame(seq(as.POSIXct(year_start), as.POSIXct(year_end), by="1 hour"))
names(date_hourly) = "Date"
date_hourly$hourly_step = c(1:length(date_hourly$Date))
date_hourly$Date = as.Date(date_hourly$Date)
start_date_in_hours = dplyr::filter(date_hourly, Date == off$Date)
off = round(mean(start_date_in_hours$hourly_step), digits = 0)
```

As soon as the melt period is set, QG is calculated on the basis of ERA over the melt period.

```
QG_era <- Rn_era[as.numeric(bp_1):off] + era5$QH[as.numeric(bp_1):off] + era5$QE[as.numeric(bp_1):off] - Qmeltterm_era[as.numeric(bp_1):off]
```

After that, elevation-corrected air temperatures and air pressures are implemented. These are joined by matching lon/lat-coordinates.

```
lat_cor = round(mod_coordinates$y, digits = 3)
lon_cor = round(mod_coordinates$x, digits=3)
dgmlst = paste0("era5_",year,"_hourly_",lalat,"_",lolon,"_Tair.csv")
folder_elevcor = paste0("/data/scratch/kemperta/MA/Height_correction/ERA5/",year,"/")
setwd(folder_elevcor)
era_Tair = read.csv(dgmlst)
era_Tair = era_Tair[,3]
dgmpair = paste0("era5_",year,"_hourly_",lalat,"_",lolon,"_Pair.csv")
era_Pair = read.csv(dgmpair)
era_Pair = era_Pair[,3]
Psurf = era_Pair \cdot 100
T_z = era_Tair
rho = Psurf / (R \cdot T_z)
Tdz = era_Tair - ((100 - era5$RH)/5.)
d2m_z = Tdz
e = 6.112 * exp((17.625 *(d2m_z))/(243.04+(d2m_z))) * 100
es = 6.112 * exp((17.625 * (T_z-273.15))/(243.04+(T_z-273.15))) * 100
RH = (e / es) \cdot 100
q_z = (0.622 \cdot e)/Psurf
Td = Tsurf - ((100 - era5$RH)/5.)
Tdew_0 = Td
e = 6.112 * exp((17.625 * (Tdew_0))/(243.04+(Tdew_0))) \cdot 100
q_0 = (0.622 * e)/Psurf
```

Then, the sensible and latent heat flux are calculated.

```
Ri = (g z (T_z - T_0))/(T_z \cdot u_z^2)
Ri = as.data.frame(Ri)
Ri$Ch = ifelse(Ri <= 0, (1-58 * Ri)^0.25, (1+7 \cdot Ri)^-0.1)
Ch = Ri$Ch
Ce = 0.5 \cdot Ch

H = -(rho cp Ch k^2 u_z (T_z-T_0))/log(z/z0)^2
names(H) <- "H"

LE = -(rho L Ce k^2 u_z (q_z-q_0))/log(z/z0)^2      #
names(LE) = "LE"
```

In addition to that, a new Q_{net} is calculated. Now, it is based on the SW_{down} and the MODIS albedo as well as LW_{net}, calculated from reanalysis-based LW_{down} and the Stefan-Boltzman-Law.

```
Rn = era5$SWdown * (1-albedo) + epsilon * era5$LWdown - epsilon sbk 273.15^4
```

Before the melt flux is calculated, all input datasets are cut to length of the melt period. Than Q_{melt} is calculated and negative values set zero, since I am only interested in snow ablation. The melt energy is then accumulated in order to get the overall amount of energy available for snow melt, which can be translated into mSWE.

```
Qmelt_max = Rn_max + H_max + LE_max - median_QG_era_max

Qmelt_max[Qmelt_max <= 0] = 0
Qmelt_cum_max = cumsum(Qmelt_max)
Qmeltera_cum_max = cumsum(Qmeltterm_era_max)
SWE_max = (Qmelt_max/Lfus) * (3600)
SWE_max = SWE_max/1000
```

A1 Supportive material

Table A1. Variables in the SEB-scheme. List of fixed parameters used in the SEB-scheme.

Variable	Symbol	Value	Unit
specific gas constant for dry air	R	287.058	$J \cdot Kg^{-1} \cdot K^{-1}$
latent heat of fusion	L_{fus}	$334 \cdot 10^3$	$J \cdot Kg^{-1}$
roughness length	z_0	$5 \cdot 10^{-4}$[a]	m
specific heat of air	c_p	1005.7	$J \cdot Kg^{-1} \cdot K^{-1}$
latent heat of vaporization	L_{vap}	$2501 \cdot 10^3$	$J \cdot Kg^{-1}$
Stefan-Boltzmann-Constant	σ	$5.67 \cdot 10^{-8}$[b]	$W \cdot m^{-2} \cdot K^{-4}$
emissivity of snow	ϵ	0.985[c]	$W \cdot m^{-2} \cdot K^{-4}$

[a] Langer et al. (2011)
[b] Tarboton et al. (1996)
[c] Langer et al. (2011); Zhang (2005)

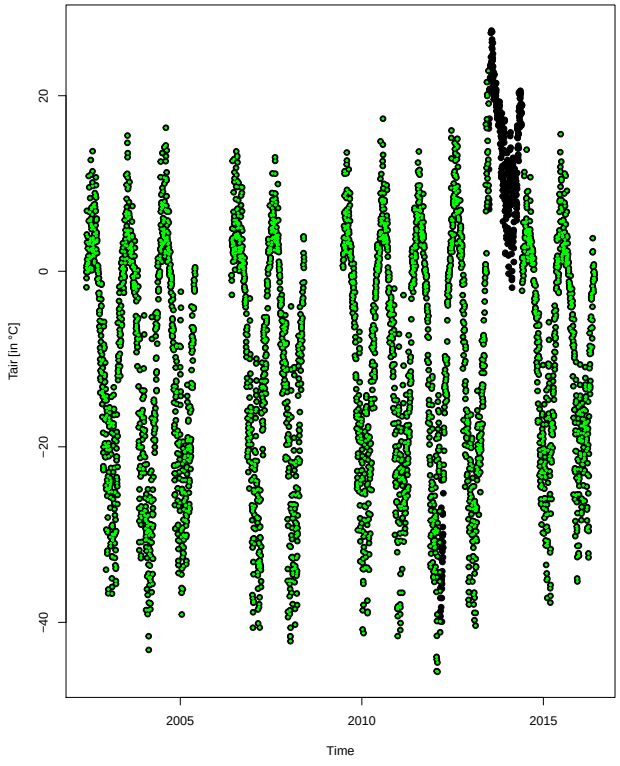

Figure A1. Observed Tair in West Dock. This graph shows the measured air temperatures at the West Dock site in black and the same data set after elimination of months containing observations that de- or exceeded the monthly average by $\pm$ 10K in green.

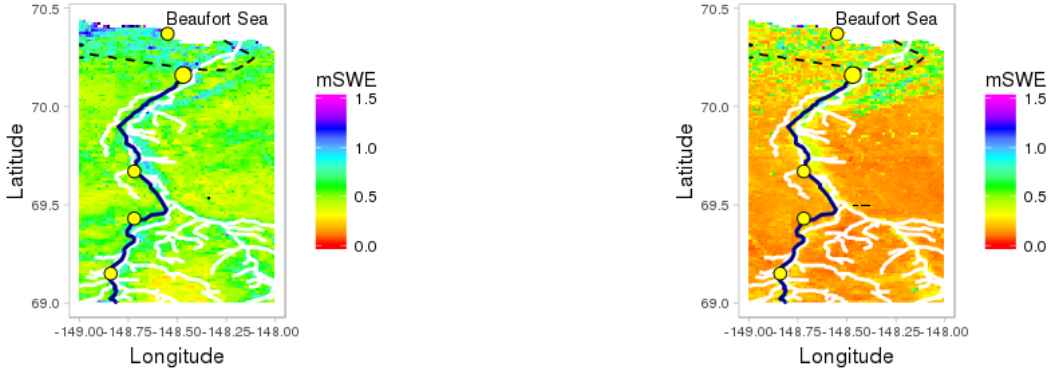

Figure A2. Comparison SWE in two consecutive years. This graph shows the peak-SWE values for the two years 2014 and 2015, respectively. As mentioned in Section 5.3, large interannual differences in snow measurements can occur between two years. On the left side, the year 2014 displays peak-SWE values, which nearly reach 1 mSWE, whereas on the right side in 2015 peak-SWE values are below 0.5 mSWE in many parts of the study area.

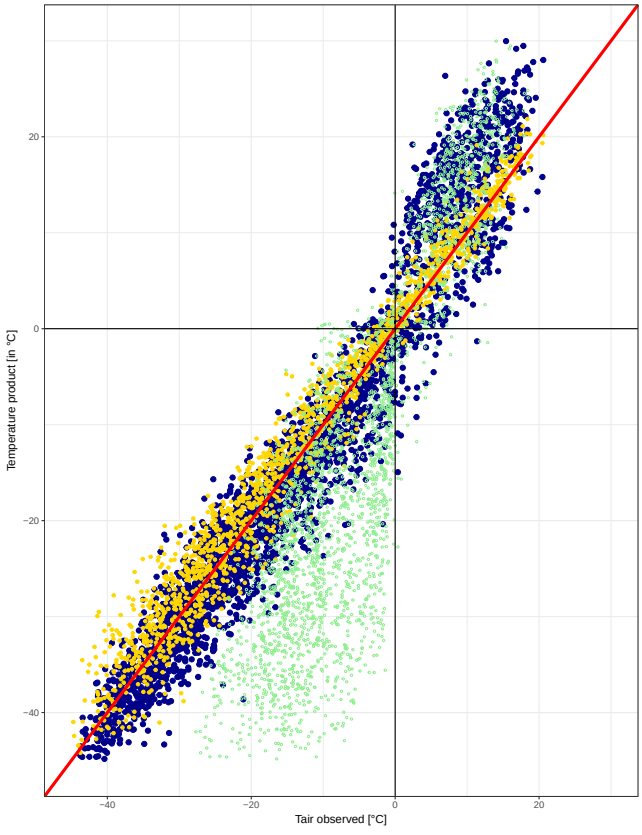

Figure A3. Scatterplot with Tair and Tsurf. This scatterplot is the same as in Figure 5, plus the comparison of ground surface temperatures with MODIS LST.

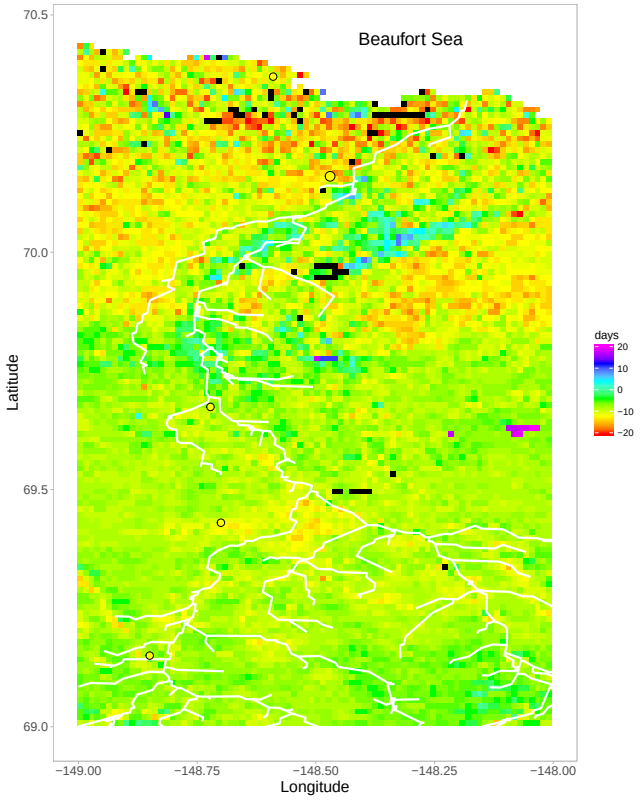

Figure A4. Snow-offset day trend 2003-2016. This graph shows the trend of snow-offset dates based on MODIS. The largest alterations in snow-offset dates is displayed for northern part of the study. As this is also the region with lower permafrost temperatures, this may reveal an increased warming in these areas compared, for instance, to the southern part of the study area.

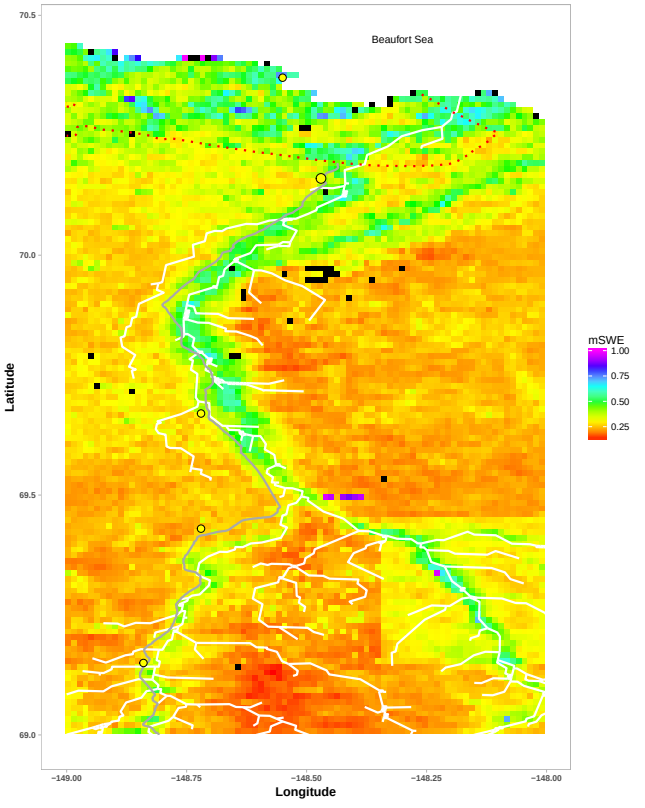

Figure A5. Average peak-SWE from 2010-2016. This average is based on the ERA-5-covered time series. On average, SWE values have been found to be larger in the coastal area and next to the Saganavirktok River. The SEB-scheme reveals comparably low SWE values for the foothills of the Brooks Range. In addition to that, this graph shows an abnormality arising by implementing the ERA-5 2010 dataset, which highlights the grid on the bottom right. Due to this, for instance, the time series in Figure 16 only contains the years 2011-2016.

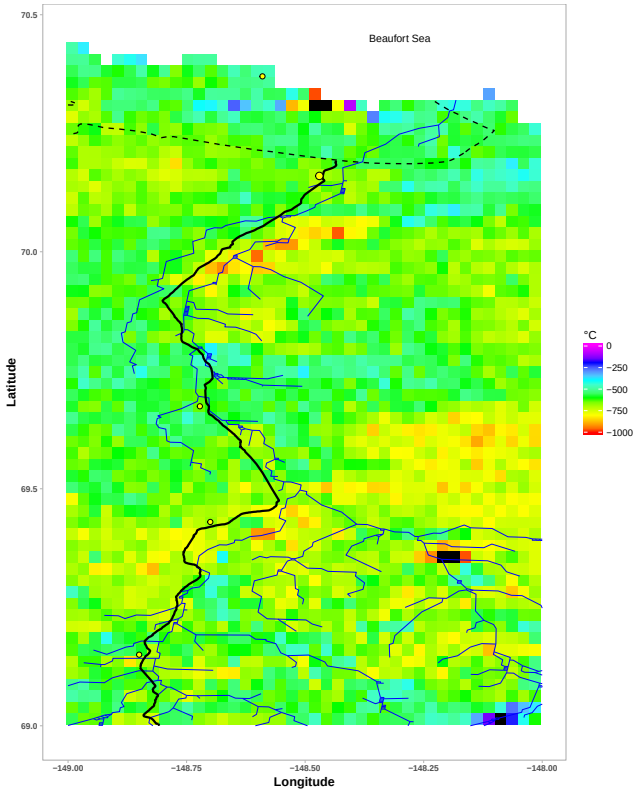

Figure A6. FDD trend snow-covered season. FDD in the snow-covered season (October till May) are demonstrated to decrease in the entire study area. As the basis is an absolute value, a decreasing FDD means a warming trend.

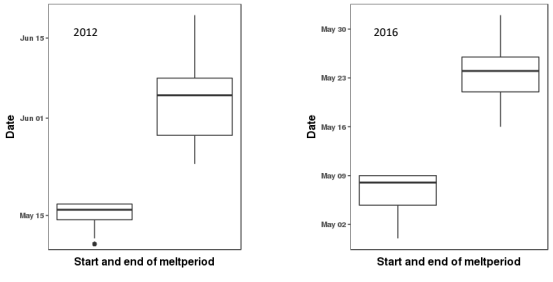

Figure A7. SEB-scheme meltperiod comparison. The melt periods derived from the SEB-scheme show a clear tendency to earlier complete snowmelt. But, it is not only the offset-date, which happens earlier in the year. The length of the melt period also show a decreasing trend.

References

Aalstad, K., Westermann, S., Schuler, T. V., Boike, J., and Bertino, L.: Ensemble-based assimilation of fractional snow covered area satellite retrievals to estimate snow distribution at a high Arctic site, 2017.

Anisimov, O. A. and Nelson, F. E.: Permafrost distribution in the Northern Hemisphere under scenarios of climatic change, Global and Planetary Change, 14, 59–72, 1996.

Anisimov, O. A., Vaughan, D. G., Callaghan, T. V., Furgal, C., Marchant, H., Prowse, T. D., Vilhjálmsson, H., and Walsh, J. E.: Polar regions (arctic and antarctic), Climate change, 15, 653–685, 2007.

Clow, G. D.: Temperature data acquired from the DOI/GTN-P Deep Borehole Array on the Arctic Slope of Alaska, 1973-2013, Earth System Science Data, 6, 201, 2014.

Dee, D. P., Uppala, S., Simmons, A., Berrisford, P., Poli, P., Kobayashi, S., Andrae, U., Balmaseda, M., Balsamo, G., Bauer, d. P., et al.: The ERA-Interim reanalysis: Configuration and performance of the data assimilation system, Quarterly Journal of the royal meteorological society, 137, 553–597, 2011.

Frei, A., Tedesco, M., Lee, S., Foster, J., Hall, D. K., Kelly, R., and Robinson, D. A.: A review of global satellite-derived snow products, Advances in Space Research, 50, 1007–1029, 2012.

Gao, L., Bernhardt, M., and Schulz, K.: Elevation correction of ERA-Interim temperature data in complex terrain, Hydrology and Earth System Sciences, 16, 4661, 2012.

Goodrich, L.: The influence of snow cover on the ground thermal regime, Canadian geotechnical journal, 19, 421–432, 1982.

Hachem, S., Allard, M., and Duguay, C.: Using the MODIS land surface temperature product for mapping permafrost: an application to Northern Quebec and Labrador, Canada, Permafrost and Periglacial Processes, 20, 407–416, 2009.

Hachem, S., Duguay, C., and Allard, M.: Comparison of MODIS-derived land surface temperatures with ground surface and air temperature measurements in continuous permafrost terrain, The Cryosphere, 6, 51, 2012.

Hall, D. K. and Riggs, G. A.: Accuracy assessment of the MODIS snow products, Hydrological processes, 21, 1534–1547, 2007.

Jafarov, E. E., Marchenko, S. S., and Romanovsky, V.: Numerical modeling of permafrost dynamics in Alaska using a high spatial resolution dataset, The Cryosphere, 6, 613–624, 2012.

Jones, B. M., Grosse, G., Arp, C., Jones, M., Walter Anthony, K., and Romanovsky, V.: Modern thermokarst lake dynamics in the continuous permafrost zone, northern Seward Peninsula, Alaska, Journal of Geophysical Research: Biogeosciences, 116, 2011.

Jorgenson, M., Yoshikawa, K., Kanevskiy, M., Shur, Y., Romanovsky, V., Marchenko, S., Grosse, G., Brown, J., and Jones, B.: Permafrost characteristics of Alaska, in: Proceedings of the Ninth International Conference on Permafrost, vol. 29, pp. 121–122, University of Alaska: Fairbanks, 2008.

Jorgenson, M. T., Racine, C. H., Walters, J. C., and Osterkamp, T. E.: Permafrost degradation and ecological changes associated with a warmingclimate in central Alaska, Climatic change, 48, 551–579, 2001.

Jorgenson, M. T., Shur, Y. L., and Pullman, E. R.: Abrupt increase in permafrost degradation in Arctic Alaska, Geophysical Research Letters, 33, 2006.

Kustas, W. P., Rango, A., and Uijlenhoet, R.: A simple energy budget algorithm for the snowmelt runoff model, Water Resources Research, 30, 1515–1527, 1994.

Lachenbruch, A. H., Sass, J., Marshall, B., and Moses, T.: Permafrost, heat flow, and the geothermal regime at Prudhoe Bay, Alaska, Journal of Geophysical Research: Solid Earth, 87, 9301–9316, 1982.

Langer, M., Westermann, S., Muster, S., Piel, K., and Boike, J.: The surface energy balance of a polygonal tundra site in northern Siberia-part 1: Spring to fall, The Cryosphere, 5, 151, 2011.

Langer, M., Westermann, S., Heikenfeld, M., Dorn, W., and Boike, J.: Satellite-based modeling of permafrost temperatures in a tundra lowland landscape, Remote Sensing of Environment, 135, 12–24, 2013.

Lindsay, C., Zhu, J., Miller, A. E., Kirchner, P., and Wilson, T. L.: Deriving snow cover metrics for Alaska from MODIS, Remote Sensing, 7, 12 961–12 985, 2015.

Ling, F. and Zhang, T.: Impact of the timing and duration of seasonal snow cover on the active layer and permafrost in the Alaskan Arctic, Permafrost and Periglacial Processes, 14, 141–150, 2003.

Liu, Y., Key, J. R., Frey, R. A., Ackerman, S. A., and Menzel, W. P.: Nighttime polar cloud detection with MODIS, Remote sensing of environment, 92, 181–194, 2004.

Molotch, N. P. and Margulis, S. A.: Estimating the distribution of snow water equivalent using remotely sensed snow cover data and a spatially distributed snowmelt model: A multi-resolution, multi-sensor comparison, Advances in Water Resources, 31, 1503–1514, 2008.

Morris, E.: Turbulent transfer over snow and ice, Journal of Hydrology, 105, 205–223, 1989.

Osterkamp, T.: A thermal history of permafrost in Alaska, in: Proceedings of the 8th International Conference on Permafrost, vol. 2, pp. 863–868, AA Balkema Publishers, 2003a.

Osterkamp, T.: Establishing long-term permafrost observatories for active-layer and permafrost investigations in Alaska: 1977–2002, Permafrost and Periglacial Processes, 14, 331–342, 2003b.

Osterkamp, T.: A thermal history of permafrost in Alaska, in: Proceedings of the 8th International Conference on Permafrost, vol. 2, pp. 863–868, AA Balkema Publishers, 2003c.

Osterkamp, T.: The recent warming of permafrost in Alaska, Global and Planetary Change, 49, 187–202, 2005.

Osterkamp, T. and Romanovsky, V.: Evidence for warming and thawing of discontinuous permafrost in Alaska, Permafrost and periglacial Processes, 10, 17–37, 1999.

Osterkamp, T., Viereck, L., Shur, Y., Jorgenson, M., Racine, C., Doyle, A., and Boone, R.: Observations of thermokarst and its impact on boreal forests in Alaska, USA, Arctic, Antarctic, and Alpine Research, pp. 303–315, 2000.

Panda, S. K., Prakash, A., Solie, D. N., Romanovsky, V. E., and Jorgenson, M. T.: Remote sensing and field-based mapping of permafrost distribution along the Alaska Highway corridor, interior Alaska, Permafrost and Periglacial Processes, 21, 271–281, 2010.

Panda, S. K., Marchenko, S. S., and Romanovsky, V. E.: High-resolution permafrost modeling in Denali National Park and Preserve, National Park Service Report NPS/CAKN/NRTR–2014/858, 2014.

Pulliainen, J.: Mapping of snow water equivalent and snow depth in boreal and sub-arctic zones by assimilating space-borne microwave radiometer data and ground-based observations, Remote sensing of Environment, 101, 257–269, 2006.

Raynolds, M. K., Walker, D. A., Ambrosius, K. J., Brown, J., Everett, K. R., Kanevskiy, M., Kofinas, G. P., Romanovsky, V. E., Shur, Y., and Webber, P. J.: Cumulative geoecological effects of 62 years of infrastructure and climate change in ice-rich permafrost landscapes, Prudhoe Bay Oilfield, Alaska, Global change biology, 20, 1211–1224, 2014.

Rittger, K., Painter, T. H., and Dozier, J.: Assessment of methods for mapping snow cover from MODIS, Advances in Water Resources, 51, 367–380, 2013.

Romanovsky, V., Sergueev, D., and Osterkamp, T.: Temporal variations in the active layer and near-surface permafrost temperatures at the long-term observatories in northern Alaska., 2003.

Romanovsky, V., Marchenko, S., Daanen, R., Sergeev, D., and Walker, D.: Soil climate and frost heave along the permafrost/ecological North American Arctic transect, in: Proceedings of the Ninth International Conference on Permafrost, vol. 2, pp. 1519–1524, Institute of Northern Engineering: Fairbanks, AK, 2008.

Romanovsky, V. E., Smith, S. L., and Christiansen, H. H.: Permafrost thermal state in the polar Northern Hemisphere during the international polar year 2007–2009: a synthesis, Permafrost and Periglacial processes, 21, 106–116, 2010.

Schuur, E. A. and Abbott, B.: Climate change: High risk of permafrost thaw, Nature, 480, 32–33, 2011.

Smith, S., Romanovsky, V., Lewkowicz, A., Burn, C., Allard, M., Clow, G., Yoshikawa, K., and Throop, J.: Thermal state of permafrost in North America: a contribution to the international polar year, Permafrost and Periglacial Processes, 21, 117–135, 2010.

Stone, R. S., Dutton, E. G., Harris, J. M., and Longenecker, D.: Earlier spring snowmelt in northern Alaska as an indicator of climate change, Journal of Geophysical Research: Atmospheres, 107, 2002.

Stuefer, S., Homan, J., Youcha, E., Kane, D., and Gieck, R.: Snow Survey Data for the Central North Slope Watershed: Spring 2012, University of Fairbanks, Water and Environmental Research Center, Report INE/WERC 12.22, 38pp., 2012.

Sturm, M. and Holmgren, J.: Effects of microtopography on texture, temperature and heat flow in Arctic and sub-Arctic snow, Annals of glaciology, 19, 63–68, 1994.

Tarboton, D. G., Luce, C. H., et al.: Utah energy balance snow accumulation and melt model (UEB), Utah Water Research Laboratory, 1996.

Van Everdingen, R. O.: Multi-language glossary of permafrost and related ground-ice terms in Chinese, English, French, German, Icelandic, Italian, Norwegian, polish, Romanian, Russian, Spanish, and Swedish, International Permafrost Association, Terminology Working Group, 1998.

Walker, D., Auerbach, N., Bockheim, J., Chapin III, F., Eugster, W., King, J., McFadden, J., Michaelson, G., Nelson, F., Oechel, W., et al.: Energy and trace-gas fluxes across a soil pH boundary in the Arctic, Nature, 394, 469, 1998.

Walker, D. A.: Hierarchical subdivision of Arctic tundra based on vegetation response to climate, parent material and topography, Global change biology, 6, 19–34, 2000.

Wan, Z.: MODIS land-surface temperature algorithm theoretical basis document (LST ATBD), Institute for Computational Earth System Science, Santa Barbara, 75, 1999.

Wan, Z.: New refinements and validation of the collection-6 MODIS land-surface temperature/emissivity product, Remote sensing of Environment, 140, 36–45, 2014.

Wan, Z. and Dozier, J.: A generalized split-window algorithm for retrieving land-surface temperature from space, IEEE Transactions on geoscience and remote sensing, 34, 892–905, 1996.

Wan, Z., Zhang, Y., Zhang, Q., and Li, Z.-L.: Quality assessment and validation of the MODIS global land surface temperature, International Journal of Remote Sensing, 25, 261–274, 2004.

Wan, Z., Hook, S., and Hulley, G.: MOD11A1 MODIS-/Terra Land Surface Temperature/Emissivity Daily L3 Global 1km SIN Grid V006[Data set], NASA EOSDIS LP DAAC, https://doi.org/10.5067/MODIS/MOD11A1.006, 2015a.

Wan, Z., Hook, S., and Hulley, G.: MYD11A1 MODIS/Aqua Land Surface Temperature/Emissivity Daily L3 Global 1km SIN Grid V006 [Data set], NASA EOSDIS LP DAAC, https://doi.org/10.5067/MODIS/MYD11A1.006, 2015b.

Westermann, S., Langer, M., and Boike, J.: Spatial and temporal variations of summer surface temperatures of high-arctic tundra on Svalbard—implications for MODIS LST based permafrost monitoring, Remote Sensing of Environment, 115, 908–922, 2011.

Westermann, S., Schuler, T., Gisnås, K., and Etzelmüller, B.: Transient thermal modeling of permafrost conditions in Southern Norway, The Cryosphere, 7, 719, 2013.

Westermann, S., Østby, T., Gisnås, K., Schuler, T., and Etzelmüller, B.: A ground temperature map of the North Atlantic permafrost region based on remote sensing and reanalysis data, The Cryosphere, 9, 1303–1319, 2015.

Westermann, S., Langer, M., Boike, J., Heikenfeld, M., Peter, M., Etzelmüller, B., and Krinner, G.: Simulating the thermal regime and thaw processes of ice-rich permafrost ground with the land-surface model CryoGrid 3, Geoscientific Model Development Discussions, 9, 523–546, 2016.

Westermann, S., Peter, M., Langer, M., Schwamborn, G., Schirrmeister, L., Etzelmüller, B., and Boike, J.: Transient modeling of the ground thermal conditions using satellite data in the Lena River delta, Siberia, The Cryosphere, 11, 1441, 2017.

Zhang, T.: Influence of the seasonal snow cover on the ground thermal regime: An overview, Reviews of Geophysics, 43, 2005.

Zhang, T., Osterkamp, T., and Stamnes, K.: Some characteristics of the climate in northern Alaska, USA, Arctic and Alpine Research, pp. 509–518, 1996.

Zhang, T., Osterkamp, T., and Stamnes, K.: Effects of climate on the active layer and permafrost on the North Slope of Alaska, USA, Permafrost and Periglacial Processes, 8, 45–67, 1997.

Zhang, Y., Olthof, I., Fraser, R., and Wolfe, S. A.: A new approach to mapping permafrost and change incorporating uncertainties in ground conditions and climate projections, The Cryosphere, 8, 2177–2194, 2014.